Master's thesis

2021

Martin Lima

NTNU
Norwegian University of
Science and Technology
Faculty of Information Technology and Electrical
Engineering
Department of Electronic Systems

Martin Lima

Design and Fabrication of 12 GHz Double Loop M-FSS Transmitarray

July 2021

NTNU
Norwegian University of
Science and Technology

NTNU
Norwegian University of
Science and Technology

NTNU

Norwegian University of
Science and Technology

Design and Fabrication of 12 GHz Double Loop M-FSS Transmitarray

Martin Lima

Electronics Systems Design and Innovation
Submission date: July 2021
Supervisor: Egil Eide
Co-supervisor: Irene Jensen

Norwegian University of Science and Technology
Department of Electronic Systems

PREFACE

This master thesis is a dive into one of the many applications of electromagnetic band gap structures (EBGs), inspired by a literature study done the previous autumn [15] where the field of EBGs and metamaterials were explored.

Any field is a world onto itself, and the question of just how an electromagnetic lens may be designed proved not to be straightforward. The focus point was long the method of using proper metamaterials and transformational optics theory, but shifted to EBGs and array theory after being acquainted with several previous works.

The framework for constructing, simulating and analyzing the numerous aspects of transmitarrays came to be 18 000 lines of code in the end. This took an appreciable amount of time to write and ponder, restricting the scope of the thesis, but was undoubtedly decisive in creating a thorough result.

I extends my greatest appreciations towards my supervisors, Professor Egil Eide and Irene Jensen at SINTEF for supporting me throughout this semester and allowing me to explore this exciting and interesting field of antenna engineering. In addition, I would like to thank Terje Mathiesen for assisting me performing the antenna measurements, and Finmekanisk Verksted at Faculty of Natural Sciences for exceedingly quickly manufacturing the foundation of the measurement jig.

SAMMENDRAG

Denne masteroppgaven presenterer to design av elektromagnetiske linser kalt transmitarray, laget med en senterfrekvens på 12 GHz og en brennvidde på $F = 400$ mm. Begge består av tre identiske plane lag som hver er dekket av 293 doble kvadratiske løkker arrangert i et periodisk gitter. Disse løkkene er enhetsceller og har en bredde på $\lambda/2$. Radiusen på transmitarrayene er 10 slike enhetsceller, eller 125 mm.

Hensikten til den første linsen er å kollimere den sfæriske bølgefronten fra en hornantenne. Den er fremstilt på FR4 substrat og målt i et anekoisk kammer. På grunn av høyere permittivitet i det fysiske substratet, har det fabrikkerte transmitarrayet en lavere senterfrekvens på 10.97 GHz samt en kortere brennvidde på $F = 300$ mm. Høyeste vinning er 9.43 dB (12 GHz, $F = 400$ mm) og 9.34 dB (10.97 GHz, $F = 300$ mm) for henholdsvis simulert og målt transmitarray. På den tiltenkte senterfrekvensen (12 GHz) har derimot det fabrikkerte transmitarrayet en vinning på kun 3.44 dB.

Målet for den andre linsen er å omforme hovedloben fra en hornantenne til to separate lober med retningene ($\theta = 45°$, $\phi = 0°$) og ($\theta = 45°$, $\phi = 45°$). Dette transmitarrayet er ikke fremstilt, men brukes for å demonstrere partikkelsvermoptimalisering for å oppnå ønsket fjernfelt. Algoritmen klarer å syntetisere fasefordelingen til en enkeltmatet tverrlobet linse etter 500 iterasjoner.

ABSTRACT

This thesis presents the design of two electromagnetic lenses called transmitarrays, designed with a center frequency of 12 GHz and a focus distance of $F = 400$ mm. Both consists of three stacked identical planar layers patterned with 293 double square loop periodic phase shifting unit cell, each cell having a width of $\lambda/2$. The radius of the transmitarrays are 10 unitcells or 125 mm.

The first lens collimates the spherical wavefront from a horn antenna. It is fabricated on FR4 substrate and measured in an anechoic chamber. Due to increased permittivity in the physical substrate, the realized transmitarray has a lower center frequency of 10.97 GHz and a shorter focus distance of $F = 300$ mm. Peak gains are 9.43 dB (12 GHz, $F = 400$ mm) and 9.34 dB (10.97 GHz, $F = 300$ mm) for the simulated and measured transmitarray, respectively. However, at the designed 12 GHz frequency and $F = 400$ mm focus distance, the realized transmitarray has a gain of just 3.44 dB.

The second lens transforms the single main lobe of a horn antenna into two separate lobes directed into ($\theta = 45°$, $\phi = 0°$) and ($\theta = 45°$, $\phi = 45°$). This lens is not fabricated, but demonstrates particle swarm optimization to achieve an arbitrary desired farfield. The algorithm manages to synthesize the phase distribution of the single-fed dual-lobe lens after 500 iterations.

CONTENTS

1 INTRODUCTION 1

2 THEORY 2
2.1 Introduction to Antenna Theory . . . 2
2.1.1 Impedance and Reactivity . . . 4
2.1.2 Nearfield and Farfield . . . 4
2.1.3 Radiation Pattern and Antenna Characteristics . . . 5
2.2 Lens Antennas . . . 8
2.2.1 Fast and Slow Waves . . . 8
2.2.2 Constrained Lenses . . . 8
2.2.3 Dielectric Lenses . . . 9
2.2.4 Artificial Dielectric Lenses . . . 10
2.2.5 Transmitarray antennas . . . 12
2.3 Transmit Arrays . . . 14
2.3.1 Array Theory . . . 14
2.3.2 The Phase Distribution . . . 17
2.3.3 Overall Performance . . . 18
2.3.4 Feed Antenna . . . 21
2.4 EBG and Unit Cells . . . 23
2.4.1 Electromagnetic Wave Parameters . . . 23
2.4.2 Periodicity and Band Gaps . . . 27
2.4.3 Limit on Layers . . . 31
2.5 Particle Swarm Optimization . . . 37
2.5.1 Functional Description . . . 37

3 DESIGN AND IMPLEMENTATION 39
3.1 Feed . . . 39
3.1.1 Feed Selection . . . 39
3.1.2 Feed Characterization . . . 41
3.2 Surface . . . 43
3.2.1 Focus Distance . . . 44
3.2.2 Surface Diameter . . . 44
3.3 Unitcell Selection . . . 47
3.3.1 Substrate . . . 47
3.3.2 Element Type Selection . . . 47
3.3.3 Double Loop Unit Cell . . . 49
3.3.4 Number of Layers . . . 52
3.3.5 Final Unit Cell Simulation . . . 52
3.4 Phase Distribution . . . 54
3.4.1 Phase Distribution 1. . . . 54
3.4.2 Phase Distribution 2. . . . 58
3.5 Assembly . . . 62
3.5.1 Structural Support . . . 62
3.5.2 Surface Suspension . . . 63
3.5.3 The Final Transmitarray . . . 64

4 MEASUREMENT METHOD 65
4.1 Test Fixture 65

5 RESULTS - SIMULATION AND MEASUREMENT 68
5.1 Gain at Designed Focus Distance 69
5.1.1 Gain at other Frequencies 70
5.2 Directivity and Gain at other Focus Distances 71

6 DISCUSSION 75

7 CONCLUSION 77

8 FUTURE WORK 78

I Appendix 79

A DERIVATION OF TRANSMISSION COEFFICIENT FOR IDEAL UNIT-CELLS 80

B SIMULATION RESULTS FOR ONE LAYER UNIT CELLS WITH ONLY METAL LAYER 82

BIBLIOGRAPHY 84

ACRONYMS

EBG	electromagnetic band gap
EM	electromagnetic
FLA	filter lens array
FSS	frequency selective surface
GRIN	gradient-index
HPBW	half power beam width
M-FSS	multilayered frequency selective surface
MTM	metamaterial
PBG	photonic band gap
PMC	perfect magnetic conductor
PSO	particle swarm optimization
PSS	phase shifting surface
TO	transformational optics

1

INTRODUCTION

Electromagnetic lenses are used to modify the wavefront of antennas [19]. This could be everything from correcting the amplitude taper of a horn antenna, to achieving active beam steering using only a single antenna element. The former was achieved in the 1940's with *constrained lenses* made from stacked metal plates, while latter has only recently been possible through electromagnetic band gap (EBG) structures and metamaterials.

This thesis aims to design, fabricate and analyze a type of electromagnetic lens called a *transmitarray*, constructed with phase shifting elements named multilayered frequency selective surface (M-FSS). The width and length of these elements are $\lambda/2$ at the design frequency of 12 Ghz, placing them in the group of EBG structures. Research into these structures and the concept of transmitarrays has had a substantial growth since the early 2000 and especially the last decade, on which this thesis is largely based.

The design goal of this thesis is twofold. The primary objective is to construct a transmitarray that collimates[1] the fields from a feed antenna in the direction normal to the surface of the transmitarray. This is analogous to an ordinary collimating optical lens. The secondary objective is to use numerical optimization to design a single-fed multi-beam transmitarray that transforms the spherical input wave into two beams aimed 90° relative to each other, so as to demonstrate the flexibility of transmitarrays.

1 I.e. make a spherical wave into a plane wave.

2

THEORY

This chapter is structured into three main parts: the history and usefulness of lens antennas; the theory of the main subject, transmitarrays; and theory of the parts, the EBG unitcells. In addition, a primer of necessary antenna theory is given at the beginning for those who may be unfamiliar with the subject. Finally, a brief explanation of a numerical technique used to synthesize transmitarrays that achieve a desired farfield is laid out at the end.

For easier page turning, the respective theory sections are found at:

p. 8, Lens antennas

p. 14, Transmitarrays

p. 23, electromagnetic band gap

p. 37, Numerical optimization

2.1 INTRODUCTION TO ANTENNA THEORY

Antennas are transitional structures between free space and a guiding device, the latter often being a coaxial cable or a hollow conductor where waves are contained within [4][1]. The transitional structures can take widely different forms, but all rely on Ampère's law that accelerating and decelerating electric charges causes electromagnetic radiation, akin to a rock thrown in a pond causes ripples in the water.

Continuously accelerating and decelerating electric charges in form of an oscillating current is the most practical way to drive an antenna. If the oscillation is a perfect sinusoidal wave, see Figure 1, it can be characterized by the frequency f and the wavelength λ. They are related by the speed of the wave v_p:

$$f \cdot \lambda = v_p. \tag{1}$$

1 The majority of this section is based primarily on [4].

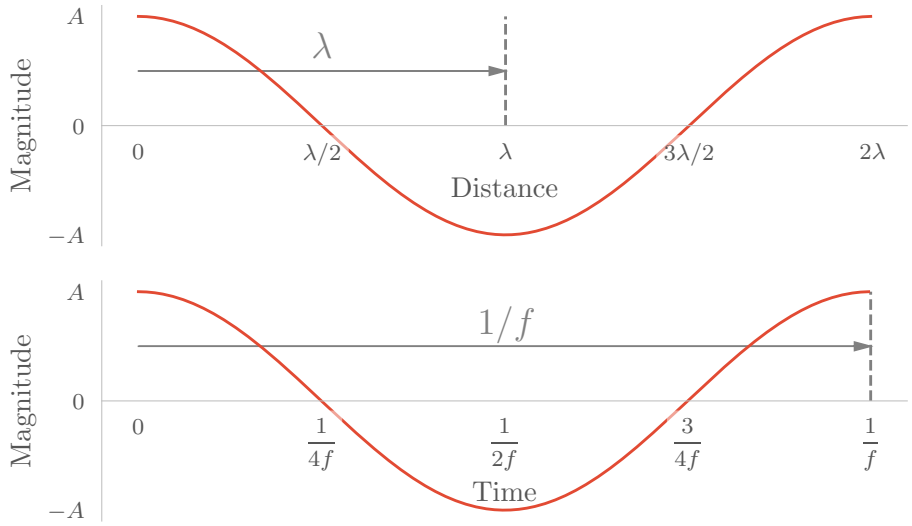

Figure 1: Illustration of an ideal sinusoid in both the spatial domain and time domain. The amplitude of the sinusoid is A and only one period is shown. The units are arbitrary.

The phase velocity v_p depends on the medium where the electromagnetic wave is propagating. In a vacuum, v_p is equal to the speed of light c. In other materials, the phase velocity can be written as a function of the fundamental constitutive parameters: the *relative permittivity* ε_r, and *relative permeability* μ_r. Permittivity is a material's resistance to alter its internal electric field in response to a changing external field. Zero resistance corresponds to $\epsilon = 1$, an example of which is vacuum, while absence of any internal field corresponds to $\epsilon = \infty$, a perfect conductor. Similarly, the permeability is the resistance against change of an internal magnetic field. Their relation with phase velocity is:

$$v_p = \frac{c}{\sqrt{\varepsilon_r \mu_r}} \tag{2}$$

A final useful relation for describing a wave propagating in a medium is the *index of refraction* $\eta = \frac{c}{v} = \sqrt{\epsilon_r \mu_r}$. This is a dimensionless number describing how many times slower an electromagnetic wave travels in a given medium relative to vacuum.

2.1.1 *Impedance and Reactivity*

The electromagnetic wave that propagates from an antenna always consists of waves in two fields: the electric field[2] $\vec{E}$ and magnetic field $\vec{H}$. We describe the relationship between these as *impedance*, Z, often specified as *wave impedance* when dealing with waves:

$$Z = \frac{\left|\vec{E}\right|}{\left|\vec{H}\right|}. \tag{3}$$

The wave impedance is a complex number where the magnitude $|Z|$ describes the difference in field intensities and the angle $\angle Z$ is the phase difference between the electric and magnetic wave. The presence of such a phase shift is due to a non-zero imaginary part of Z.

The imaginary component of Z is named *reactance*. In short, this relates to how much energy is stored in the field and not radiated away during one oscillation. During half of one oscillation, energy is dumped into the fields, only to subsequently be taken away during the second half of the oscillation.

2.1.2 *Nearfield and Farfield*

The field distributions close to an antenna behaves differently than those far away. Different spatial regions around antennas are therefore defined. These are *reactive near-field* where the reactive part of the fields are large; *radiating near-field*[3] where the angular components of $\vec{E}$ and $\vec{H}$ are dependent of distance; and the *far-field*[4] where the angular component of field distributions are independent of distance.

The key take away from the different field regions is that the far-field is a "nice" region. This stems from two properties. Firstly, the equations become simplified as near-field terms fall away with $1/r^n, n > 2$ with distance r. Secondly, structures and disturbances placed at the farfield does not become mutually coupled with nor change the radiation characteristics of the antenna[5].

2 Technically, these are the electric and magnetic field *intensity vectors*.
3 Radiating near-field is also called the *Fresnel* region
4 The far-field is also called the *Fraunhofer* region
5 A practical demonstration of this is when you place you hand close to an FM aerial causing deleterious effects on audio-quality, but standing beside the FM-radio results in minimal audible changes.

For an antenna where the largest dimension is D, the far-field begins at a distance:

$$r \geq \frac{2D^2}{\lambda} \tag{4}$$

2.1.3 *Radiation Pattern and Antenna Characteristics*

The *radiation field pattern* is the field strength[6] along a circle or sphere of constant radius. It is thus a spatial graph of how the antenna radiates. Equal radiation in all directions is *isotropic*, and is often used as a reference when comparing an antenna in question. Another commonly used representation is the spatial variation of power density, called a *power pattern*. An example of a field pattern of a dipole is shown in Figure 2 below.

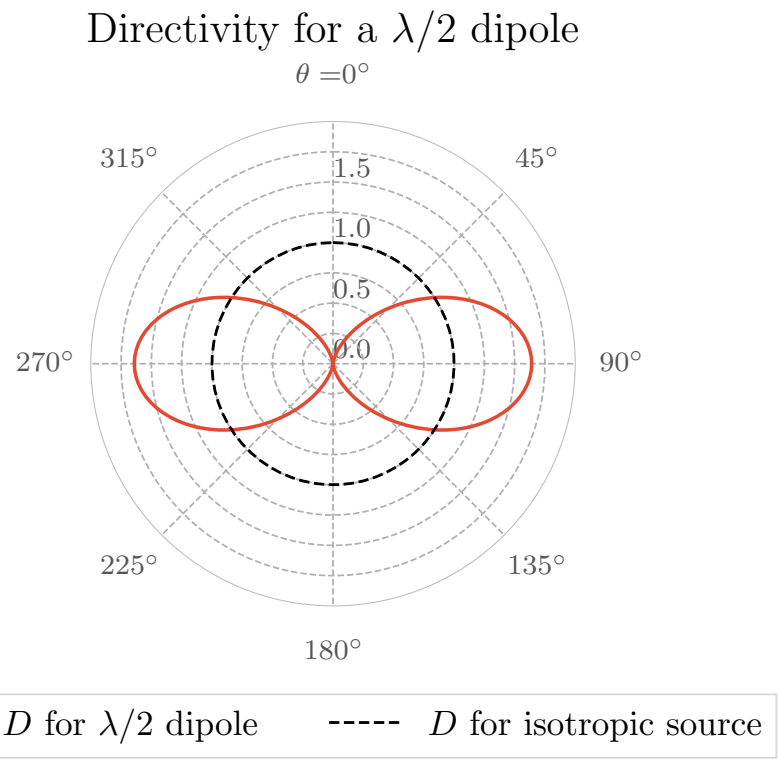

Figure 2: Radiation field pattern of a half wave dipole antenna with the field of an isotropic source inscribed. The term *half wave dipole* means that the total length of the dipole is $\lambda/2$. This length is often used in practice since it is easy to match while also giving few lobes. As can be seen from this plot, directivity is gained in the $\theta = \pm 90°$ direction, but lost in the $\theta = 0°, 180°$ directions.

6 The field may be either electric or magnetic.

The local maxima of the radiation pattern are called *lobes*[7]. The lobes of highest magnitude are the *main lobes*, while all other are termed *minor lobes*. The lobes adjacent to the main lobe are the *side lobes* . Often, there is only one intended main lobe and the strongest undesired lobe in the backward direction is called the *back lobe*.

The degree to which an antenna directs energy in a given direction is an important property, and can be indicated by an radiation pattern. This is called *directivity*, and is defined as the ratio of the radiation intensity in a given direction from the antenna to the radiation intensity averaged over all directions[4]. It is closely related with *beamwidth*, commonly defined as the width between the half power points of $\left|\vec{E}\right|^2$. If the half power beam width (HPBW) becomes narrower, the directivity will increase, and vice versa.

The expression for directivity is:

$$D = U\frac{4\pi}{P_{\text{rad}}}, \tag{5}$$

where D is directivity; U is *radiation intensity* related to the farfield by $U = \frac{r^2}{2Z_0}\left|\vec{E}\right|^2$, of which Z_0 is the intrinsic impedance of the medium $Z_0 = \sqrt{\frac{\mu}{\varepsilon}}$; and P_{rad} is the total radiated power. The latter is obtained by integrating the radiation intensity over a sphere enclosing the antenna:

$$P_{\text{rad}} = \int_0^{2\pi}\int_0^{\pi} U \cdot \sin\theta \;\, \mathrm{d}\theta\, \mathrm{d}\phi \tag{6}$$

Inserting (6) into (5) gives an alternate and commonly encountered expression for directivity:

$$D = 4\pi\frac{U}{\int_0^{2\pi}\int_0^{\pi} U \cdot \sin\theta \;\, \mathrm{d}\theta\, \mathrm{d}\phi}. \tag{7}$$

7 The fundamental cause of this "lobeyness" is the fact that the electromagnetic field has a Fourier relationship with the current distribution in the antenna.

When there is no explicit direction, "directivity" normally implies *maximum directivity* D_0. This is obtained at maximum radiation intensity $U_{\max}$, resulting in:

$$D_0 = 4\pi \frac{U_{\max}}{\int_0^{2\pi}\int_0^{\pi} U \cdot \sin\theta \ \mathrm{d}\theta\,\mathrm{d}\phi} \tag{8}$$

$$= \frac{4\pi}{\int_0^{2\pi}\int_0^{\pi} U_N \cdot \sin\theta \ \mathrm{d}\theta\,\mathrm{d}\phi}, \tag{9}$$

where U_N is normalized radiation intensity.

The last antenna characteristic that is important for the following text is *gain*, G. This is defined the same way as directivity, but with total radiated power replaced with P_{in}, the total power fed into the antenna[8]. P_{rad} is just P_{in} minus resistive and dielectric losses. These losses are captured as conduction efficiency e_c and dielectric efficiency e_d, respectively. This gives the relation:

$$G = e_c e_d D. \tag{10}$$

A final note in what (10) shows: the only way to increase the gain of any antenna, efficiencies being constant, is to increase the directivity. By (7), increasing directivity entails increasing $U_{\max}$ at the cost of decreased U in all other direction, i.e. the beamwidth must decrease if the gain of the antenna is to be increased.

2.1.3.1 *The Poynting's Vector*

The electric field does not transfer any energy by itself. Only together with its twin the magnetic field, does the propagation of energy follow. The direction and magnitude of this energy flux – energy per surface area – is called the Poynting's vector, named after its discoverer. It is defined by equation (11). The point of importance is that the Poynting's vector is by construction *always perpendicular* to both the $\vec{E}$ and $\vec{H}$, no matter the value of ϵ and μ.

$$\vec{S} = \vec{E} \times \vec{H} \tag{11}$$

8 Under the assumption that the antenna is matched.

2.2 LENS ANTENNAS

Lens antennas aim to alleviate undesired radiation characteristics by placing an object that modifies the wavefront in front of the radiating element ([30], ch.1). Such objects are called lenses because of their legitimate similarity to optical lenses. The only real differences is the wavelength of the light and the materials that are used. Both correct aberrations in the farfield by introducing varying phase delays across the surface of the lens.

A simplified summary of how lenses work can be made by modeling the path of the wavefront as discrete rays. Each ray is at any point perpendicular to the surface of the wavefront and points into direction of energy transfer. The lens is modeled as a block of material that is discretized into separate slabs. Each slab adds a certain phase delay $\Delta\phi$ to the ray that passes through it.

2.2.1 *Fast and Slow Waves*

The many different types of lenses can be categorized by whether phase delays are positive or negative when a wave is propagating through it ([30], ch.1). Lenses of the first type is by far the most common and are called *slow wave lenses*. Waves passing through these gets a $\Delta\phi > 0$ added to them, slowing them down. The opposite happens for the second type, called *fast wave lenses*. Propagating waves gets a $\Delta\phi < 0$ added, speeding them up.

Another way to express this is by using index of refraction. By the definition given in Section 2.1 above, waves propagating in a medium with $\eta > 1$ travels slower than in free space. By extension, propagating waves travels faster than in free space if $\eta < 1$. Slow wave lenses thus have a η greater than unity, while fast wave lenses has η lower than unity, even negative in some cases of metamaterials.

2.2.2 *Constrained Lenses*

Constrained lenses rely on structures that in some way constrain the wave[16][26], and it is one of the earliest examples of lens antennas. One such lens is the metal plate lens where stacked plates form waveguides of varying lengths that guide the wave, see figure 3. The behavior of constrained lenses are thus not determined by refractive index[26], differentiating them from the other antenna type.

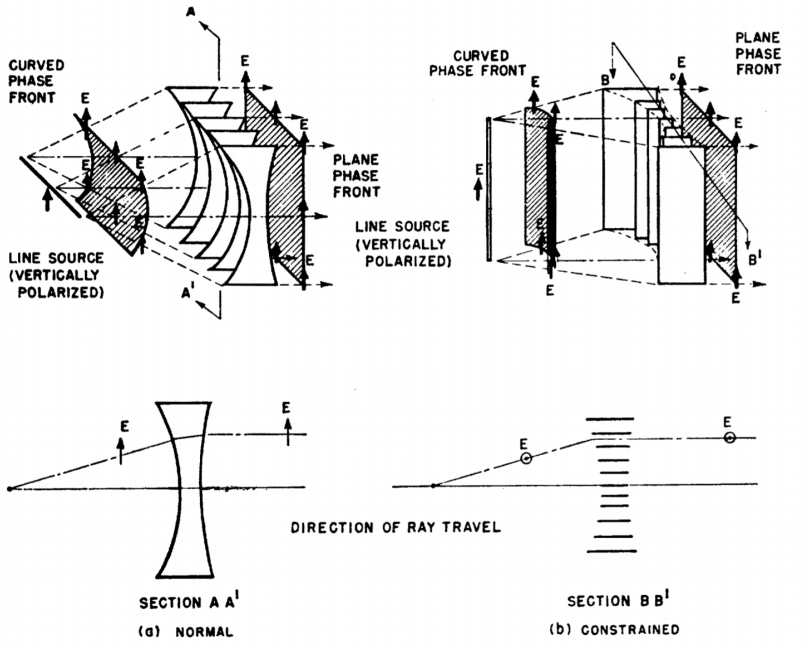

Figure 3: Illustration of two kinds of metal plate lenses, reprinted from a journal paper from 1950[26]. In a), the leftmost, is an "ordinary" lens, being describable by Snell's law. b) shows a constrained lens where the wave is guide between the plates.

2.2.3 *Dielectric Lenses*

Dielectric lenses are directly analogous to common optical lenses. They are constructed of non-conductive low loss materials that have a precise permittivity and permeability, causing a specific index of refraction by the aforementioned relation $\eta = \sqrt{\epsilon_r \mu_r}$. Normally, $\mu_r \approx 1$ and is neglected ([19], ch.9). In contrast to optical elements, the materials used at microwave frequencies are often opaque ceramics, polymers or foams ([30], ch.1). Some transparent materials like sapphire and quartz could also be used as microwave lenses[27], but rarely are on the basis of the size necessitated by the long wavelengths and their price.

Dielectric material can be used for phase shaping in two ways. The first is to vary the shape of the lens just like optical lenses. Thicker sections will induce a higher $\Delta\phi$ than thinner ones. For the normal case of $\eta > 1$, a convex shape will transform spherical a plane wave into a plane wave, collimating it, while a concave shape will transform a plane wave into a spherical wave, spreading it. In the cases of a refractive index lower than one, $\eta < 1$, it is the other way around; a convex lens will spread plane wave while a concave shape will collimate a spherical wave.

The second method of using dielectric materials to create a lens is to vary the permittivity throughout the material. These are called gradient-index (GRIN) lenses. As a true permittivity gradient is hard to manufacture, several discrete steps are used to form an approximation of the permittivity profile ([30], p.193). An example of a stepped index ceramic lens is shown in figure 4.

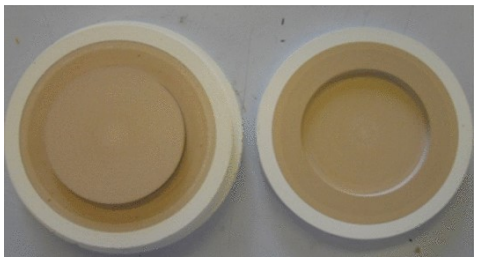

Figure 4: Example of a stepped index dielectric lens called a Luneberg lens. Each color change in this picture is a slightly changed ceramic. Several ceramic layers are poured and cast individually before assembling into the final lens. Reprinted from[17]

GRIN lenses have the advantage over shaped lenses of being more lightweight and having simpler geometry. Considerable less volume is needed if a convex shape is transformed into a flat surface. Even though the refractive index profile of stepped-index lenses can only approximate a true gradient, there is negligible performance loss if the steps are made small enough

2.2.4 *Artificial Dielectric Lenses*

Artificial dielectric lenses are an evolution of dielectric lenses where the materials are exchanged with so-called metamaterial. In contrast with natural materials like polymers and ceramics which gain their properties from their molecular composition, the electrical properties of metamaterials results mainly from their macroscopic structure [7] [5] [23]. These structures are engineered to give the material a desired response around a specified frequency band, alleviating the need for exotic materials and enabling a high degree of design freedom. An example of a metamaterial lens is shown in figure 5. The theory of metamaterials are examined in more detail in section 2.4.

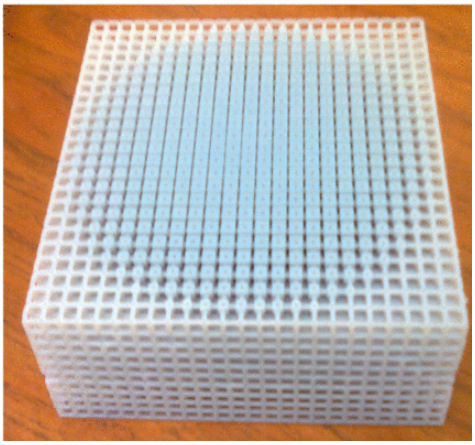

Figure 5: Cross section image of a metamaterial X-band Luneberg lens with a measured gain of 20 dB[14].

One advantage of using metamaterials is the ability of using 2D surfaces instead of 3D volumetric structures. This does not only save weight, but also enables construction by widely used planar fabrication technologies, like those for printed circuit boards. These *metasurfaces* have a great many applications, from suppressing surface waves [29] to creating cloaking devices ([7], ch.6), see figure 6 and 7 for an example of the latter.

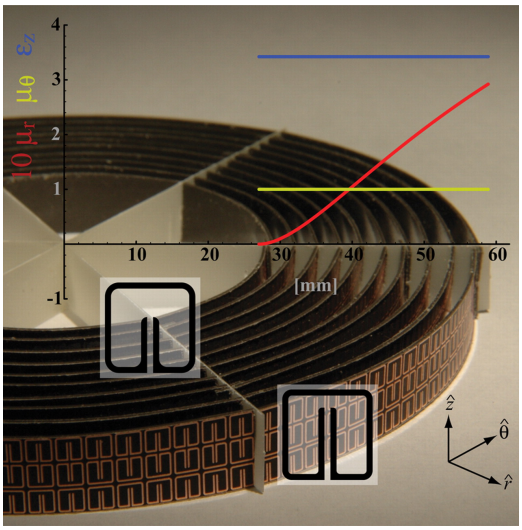

Figure 6: Image of a cloaking device designed to operate at 10 GHz [28]. It is made from layering several metasurface strips around a central cavity wherein the object to be cloaked is placed. The superimposed graph shows the permeability, μ, and permittivity η in different axes. Images of the shape of the structure elements are also superimposed.

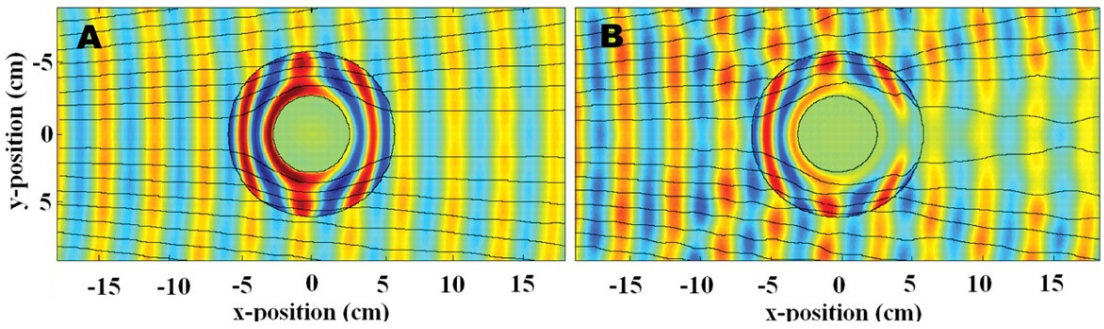

Figure 7: Simulations of the steady state electric field through the cloaking device shown in figure 6 view from the top. **A)** device with ideal material properties. **B)** device with estimated material properties [28].

2.2.5 *Transmitarray antennas*

When a planar surface is placed in front of a radiating element as a part of an antenna structure, it is called a *transmitarray*[9]. Common in all transmitarray designs is that it is composed of smaller elements called *unitcells*, often shortened to just *cells*. An important point is that the kind of surface and the kind of procedure used to design the surface differ considerably depending on the kind of cell used, but the only difference may be the size of the cell.

In terms of the guided wavelength λ_g, unitcells can be categorized in three representative types: constrained, phase shifting, or metamaterial.

The first type falls in the constrained lens category[18]. It consists of two radiating elements connected by a transmission line. The incoming wave is adsorbed by the front element, added a phase shift from the transmission line and reradiated by the back element. The theory is much the same as with an frequency selective surface (FSS)-array, but the structure and principle of operation is more similar to that of constrained lenses like rectangular waveguide lenses.

9 Transmitarrays are sometimes called *lens arrays* or *discrete lenses* ([30], p.30-31). Other authors use the more generic term phase shifting surface (PSS)[10][11] or more specific names like filter lens array (FLA)[1]

The second type, which is called phase shifting cell or frequency selective surface, have unitcell sizes up to $\lambda_g/2$. They are too large to be homogeneous and does not constitute an effective medium. Instead of using optical theory, each cell is modeled as a radiator described by S-parameters. The resultant field after illumination is calculated by summing the fields from all radiators by simple superposition. Synthesis of a field is done by finding the set of S_{21}-coefficients that give the desired field. This is followed by finding the physical cell dimensions that correspond these S_{21}-coefficients.

For the final type is the metamaterial unitcells. The size is of the order of $\lambda_g/10$, and the incoming wave can only probe the average cell properties, making the surface appear homogeneous and act like an artificial dielectric. When this is the case, *effective medium theory* can be used to model the surface ([7], p.2). The procedure to design a metamaterial lens is to utilize transformational optics theory[7][10], where a desired transformation of space is found that maps an input space – spherical wave - to an output space – a planar wave. Maxwell's equations are then used to calculate the necessary permittivities and permeabilities that achieve this transformation. Lastly, the structures of the unitcells that achieve these properties are found [8].

2.2.5.1 *Transmitarrays and Reflectarrays*

The construction of a transmitarray is in many ways similar to *reflectarrays* where a planar surface replaces a conventional reflector, removing the manufacturing complexity of a precisely curved reflector and enabling abilities like beam steering[22][12]. The reflectarray has several advantages. Firstly it is less affected by loss as the waves are not transmitted through it. Secondly, it can be made more compact as the feed illumination and reflected wave occupies the same space. Transmitarrays are on the other hand, not affected by feed blockage like reflector based antennas, and can accommodate structures like shrouds that reduce sidelobes or constrain the antenna to a lower formfactor [13].

10 There are actually three possible methods. In order of increasing complexity and ability to take into account anisotropy, they are: geometrical optics, quasi-conformal mapping and transformational optics ([8], ch.1).

2.3 TRANSMIT ARRAYS

Radiation analysis, i.e. the calculation of the farfield radiation pattern $\vec{E}$ of the transmitarray, is fundamental to calculate the array's performance and estimate the impact of errors in the structure. Throughout the following chapters, the array theory approach is used for all radiation analyses. Even though this approach does not model the feed and element polarization like aperture field analysis ([21], p.23), it is simple to formulate and lends itself to rapid computer program development and high computational speeds.

2.3.1 *Array Theory*

The farfield radiation pattern of a transmitarray illuminated by a feed F, is given by ([21], p.20) ([3], p.9)

$$\vec{E}(\hat{u}) = \sum_{n=1}^{N} E\vec{F}_n(\hat{u}) \cdot \vec{I}_n(\hat{u}) \tag{12}$$

$$\hat{u} = \sin\theta\cos\phi\ \hat{\mathbf{x}} + \sin\theta\sin\phi\ \hat{\mathbf{y}} + \cos\theta\ \hat{\mathbf{z}} \tag{13}$$

where N is the number of unitcells, $E\vec{F}_n$ is the *element factor*[11] and $\vec{I}_n$ is the *element excitation vector function* for the nth element. Both are discussed further below. Lastly, $\hat{u}$ is the unit vector pointing in the farfield direction, having elevation angle θ with the z axis and azimuth angle ϕ.

11 The element factor is also called the *element pattern* function

2.3.1.1 *Element factor*

The element factor models the farfield for *a single* unitcell. A cosine function is normally used as an approximation [21]. When all the unitcells lie in the same xy plane, the element factor will be equal for all n, and (12) may be simplified to

$$\vec{E}(\hat{u}) = \cos^{q_f}(\theta) \sum_{n=1}^{N} \vec{I}_n(\hat{u}) \tag{14}$$

$$= \cos^{q_f}(\theta) \cdot A\vec{F}_n \tag{15}$$

where $A\vec{F}_n$ is the *array factor*. The array factor models how isotropic point sources are oriented in space and how they interact with each other. Although this text will not explicitly use the array factor to great extent, students familiar with array antennas or solid state theory will recognize this expression as its basic formulation is widespread.

2.3.1.2 *Element excitation vector function*

The element excitation vector function $\vec{I}_n$ describes the field of element n in the direction $\hat{u}$. It captures two contributions: the magnitude and phase of the wave from the feed at element n, and the magnitude and phase *shift* induced by element n. The expression of $\vec{I}_n$ is shown in equation (16):

$$\vec{I}_n(\hat{u}) = T_n \cdot \vec{D}_n(\hat{u}) \tag{16}$$

$$T_n = I_{f,n} \cdot S_{11,n} \tag{17}$$

$$\vec{D}_n(\hat{u}) = e^{j\beta(\vec{r}_n \hat{u}^T)} \tag{18}$$

where T_n is a complex taper term consisting of $I_{f,n}$, the feed excitation for element n, and $S_{11,n}$, the magnitude and phase shift of element n. The second is the directional term, $\vec{D}_n$, which is calculated from $\vec{r}_n$, the vector pointing from the center of the surface to element n, and the previously defined $\hat{u}$.

2.3.1.3 *Feed Excitation Function*

The feed excitation is given by (19):

$$I_{f,n} = \alpha_n e^{-j\Psi_n} \tag{19}$$

$$\alpha_n = \frac{|F_n|}{\left\|\vec{r}_n - \vec{r}_f\right\|} \tag{20}$$

$$\Psi_n = \beta\left\|\vec{r}_n - \vec{r}_f\right\| + \phi_o. \tag{21}$$

Here, α_n is the magnitude of the feed illumination for element n, and Ψ_n is the phase of this illumination. The magnitude α_n consists a vector pointing from the feed to the nth element, $\vec{r}_f$, and the feed pattern in that direction at a distance of 1 m, F_n. The phase term, Ψ_n, is calculated from the distance between the feed and the nth element, $\left\|\vec{r}_n - \vec{r}_f\right\|$, in addition to a phase offset, ϕ_o.

The feed illumination is modeled by the farfield radiation pattern of the feed at a distance of 1 m. This 1 m normalization enables power calculations to be performed. The symbol for the value of the radiation pattern in direction (θ^f, ϕ^f) is $F(\theta^f, \phi^f)$, where the superscripts denote the feed's local coordinate system.

To allow for feed placement error analysis, the feed is rotated about all three axes. This rotation is represented by the rotation matrix R^f. Its definition and decomposition into individual rotation matrices are given in equation (22):

$$\mathbf{R} = \mathbf{R}_z\mathbf{R}_y\mathbf{R}_x \tag{22}$$

$$\mathbf{R}_x = \begin{pmatrix} 1 & 0 & 0 \\ 0 & \cos\left(\rho_x^f\right) & -\sin\left(\rho_x^f\right) \\ 0 & \sin\left(\rho_x^f\right) & \cos\left(\rho_x^f\right) \end{pmatrix} \tag{23}$$

$$\mathbf{R}_y = \begin{pmatrix} \cos\left(\rho_y^f\right) & 0 & \sin\left(\rho_y^f\right) \\ 0 & 1 & 0 \\ -\sin\left(\rho_y^f\right) & 0 & \cos\left(\rho_y^f\right) \end{pmatrix} \tag{24}$$

$$\mathbf{R}_z = \begin{pmatrix} \cos\left(\rho_z^f\right) & -\sin\left(\rho_z^f\right) & 0 \\ \sin\left(\rho_z^f\right) & \cos\left(\rho_z^f\right) & 0 \\ 0 & 0 & 1 \end{pmatrix} \tag{25}$$

where ρ^f is the rotation angle about the given axis in the feed's local coordinate system.

The resulting expression of the radiation pattern of the feed in the direction of the nth element, F_n, is calculated by simple coordinate transform:

$$\vec{r}_n^f = \mathbf{R}\left(\vec{r}_n^T - \vec{C}^T\right) \tag{26}$$

$$= \left(r_{n,x}^f, r_{n,y}^f, r_{n,z}^f\right) \tag{27}$$

$$\theta_n^f = \operatorname{acos} \frac{r_{n,x}^f}{\left\|\vec{r}_n^f\right\|} \tag{28}$$

$$\phi_n^f = \operatorname{acos} \frac{r_x^f}{\left\|\vec{r}_n^f\right\|} \tag{29}$$

$$F_n = F\left(\theta_n^f, \phi_n^f\right) \tag{30}$$

where $\vec{C}$ is the position vector of the origin of the feed.

2.3.2 *The Phase Distribution*

The phase distribution[12] is the set of individual phases for each unitcell. It constitutes the phase of the $S_{21,n}$ parameter in the complex taper function given in (17).

The phase distribution can be found by two methods. The first is to use array antenna theory to find the progressive phase distribution the creates a beam in a given direction and account for the necessary phase shift from the feed such that the beam become collimated[12]. This method will be termed the *progressive phase method* and is detailed below. The second phase distribution method is to use numerical optimization techniques to find the distribution that gives the desired farfield pattern. This thesis uses particle swarm optimization for the latter, as described in Section 2.5.

The decision to use either method depends on many factors. Firstly, the progressive phase method is extremely quick as the expression is easy to evaluate. This is in stark contrast to numerical techniques which normally require considerable time before a decent solution is found. Secondly, numerical techniques can approximate any farfield pattern and therefore be used to create lenses that correct the farfield of any antenna.

12 The phase distribution is also called the phase-shift distribution[12]

2.3.2.1 *The Progressive Phase Method*

The progressive phase method is based on the phased array expression [12] for steering a beam in direction $\hat{r}_o$:

$$\psi_n = \beta \vec{r}_n \cdot \hat{r}_o + \psi_0, \tag{31}$$

where $\psi_n = \angle S_{21,n}$ is the phase shift of the nth element, $\beta = \mathrm{Re}\{k\}$ is the real part of the wavenumber, and ψ_0 is a constant phase offset. This constant offset can be used to minimize loss when the unitcells are non-ideal as described in Section 3.4.

The expression is expanded to account for the phase delay from the feed, given as the distance from the feed to the nth element, R_n[3]:

$$\psi_n = \beta \left(R_n - \vec{r}_n \cdot \hat{r}_o \right) + \psi_0 \tag{32}$$

$$R_n = \left\| \vec{r}_n - \vec{r}_f \right\|. \tag{33}$$

The main lobe is broadside when $\vec{r}_i \cdot \hat{r}_o = 0$, and (32) gives the phase distribution that collimate the spherical wave from the feed.

2.3.3 *Overall Performance*

There are two performance measures that is used to evaluate possible transmitarray designs: directivity and spillover efficiency. The former is identical to the definition given in (5), and the latter is a measure of how much power the surface intercepts from the feed. Both are used to determine the diameter of the array and the focus distance.

2.3.3.1 *Directivity*

There is no analytical expression for the directivity of transmitarray antennas. Instead, numerical methods are used. Two such methods are used here[13] and both are described in existing literature [9]. These are respectively called *the numerical integration method* and *the Bessel method*.

13 Two methods are used to validate the accuracy of each other. A third numerical technique called the aperture efficiency method was also implemented and tested, but was consistently 3 dB higher than the other two methods and therefore abandoned.

The numerical integration method is the direct conversion of the expression in (5), iterated below in (34)-(35):

$$D_0 = \frac{U_{\max}}{U_0} = 4\pi \frac{U_{\max}}{P_{\text{rad}}} \tag{34}$$

$$= 4\pi \frac{|E(\theta_0, \phi_0)|^2}{\int_0^{2\pi} \int_0^{\pi} |E(\theta, \phi)|^2 \sin\theta \ \mathrm{d}\theta \, \mathrm{d}\phi}, \tag{35}$$

into discrete form:

$$D_0 = 4\pi \frac{|E(\theta_0, \phi_0)|^2}{\sum^{N_\theta} \sum^{N_\phi} |E(\theta, \phi)|^2 \sin\theta \ \Delta\theta\Delta\phi} \tag{36}$$

where $\Delta\theta, \Delta\phi$ are the step sizes, and N_θ, N_ϕ are the number of steps. As like other numerical methods, the result becomes more accurate for smaller step sizes, but takes more computational time.

The Bessel method is derived by rewriting the denominator of (34) in terms of Bessel functions such that the dependence of angular steps, $\Delta\theta, \Delta\phi$, disappear. This method is considerably faster to compute, but assumes that the elements are perfectly isotropic.

As the derivation is somewhat tedious and is found in other sources [9] [3], only the final expression is given here:

$$D_0 = \frac{|E(\theta_0, \phi_0)|^2}{\sum_{i=1}^{N} \sum_{j=1}^{N} T_i T_j^* \operatorname{sinc} k\rho} \tag{37}$$

$$k = \frac{2\pi}{\lambda}$$

$$\rho = \left\| \vec{r}_i - \vec{r}_j \right\| \tag{38}$$

$$\operatorname{sinc} x = \frac{\sin x}{x}, \tag{39}$$

where N is the number of elements, T_n is the complex taper function defined in (17), $*$ is the complex conjugate, k is the wavenumber, and ρ is the distance between two elements with their position vector $\vec{r}_n$.

2.3.3.2 *Spillover Efficiency*

Spillover efficiency η_s is defined as the ratio of power intercepted by the transmitarray to the total power emitted from the feed [33]:

$$\eta_s = \frac{\int_\sigma \vec{S}\ \mathrm{d}S}{\int_\Sigma \vec{S}\ \mathrm{d}S} \tag{40}$$

where $\vec{S}$ is the Poynting's vector as defined in (11), Σ is a surface enclosing the feed, and σ is the portion of Σ that illuminates the array.

In this text, the numerator of (40) is found by projecting the area of each unitcell onto the local coordinate system of the feed and multiplying this area by the power density at the center of the cell:

$$\int_\sigma \vec{S}\ \mathrm{d}S \approx \sum_{n=1}^{N} A_{\mathrm{prj},n} \cdot P_{D,n} \tag{41}$$

where $A_{\mathrm{prj},n}$ is the projected area of element n and $P_{D,n}$ is the power density at the center of that cell.

This approach has the advantage of being applicable to all feed orientations and possible arrangements of unit cells, but at the cost of not being an analytical expression like those used in literature [9].

The projected area A_n is found in three steps. First, the four corners of the unitcell are translated into the feed's coordinate system by coordinate transform. Then, these corner vectors are projected onto the feed vector $\vec{r}_{f,n}$. Lastly, Heron's formula[14] is used to calculate the area of the triangles made by the projected corner points[15].

14 Formula for finding the area of a triangle if all three sides are known.

15 Heron's formula for triangles is used instead of Bretschneider's formula for quadrilaterals since the latter requires more information than just side lengths.

2.3.4 *Feed Antenna*

The feed antenna illuminates the transmitarray surface. Even though any antenna may be used, this thesis will only use an *horn antenna* for illumination. This is a widely used type of antenna which may be found in ordinary satellite dishes to microwave calibration equipment. Its versatility stems from large gain, very high efficiency and simple construction ([4], ch.13).

A horn antenna is fundamentally a hollow rectangular or elliptical pipe that flares out, see Figure 8. In short, the flare function as a gradual transition and impedance matching of the waves propagating within the waveguide into free space.

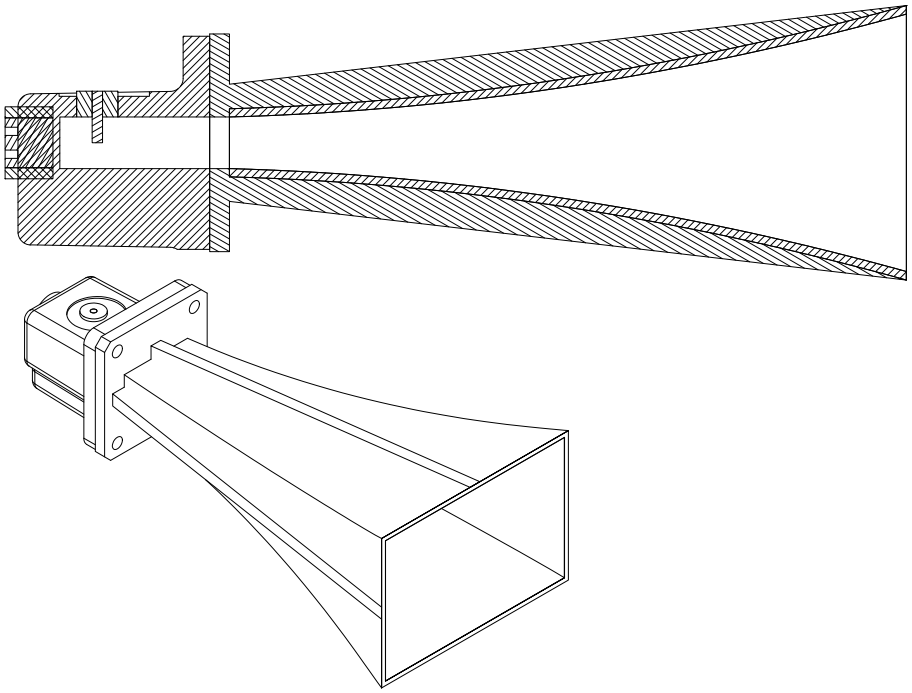

Figure 8: Illustration of a horn antenna in cross section(top) and perspective (bottom). The protrusion in the rear is the coaxial to waveguide transition. The waveguide mates with the flare of the horn which gradually expands to a wider opening.

As the feed is not central to this thesis, only a qualitative description of the effect of the flaring is considered necessary. Central in this description is the *phase error*. Since the wave expanding from the throat is spherical, there is a difference in phase at the horn's mouth between the center point and at the walls. Increasing this error decreases the gain of the horn.

Two parameters affect the phase error and are thus essential for the horn antenna: the *flare angle* between the walls and the center axis, and the length of the horn. In general, high gain is achieved the transition between the waveguide to free space is gradual. I.e. when the flare angle is shallow and the horn is long relative to the wavelength. But since increasing either the flare angle or the length increases the physical size of the antenna, there are inherent design tradeoffs that are filled by the numerous available horn antennas on the market.

2.4 EBG AND UNIT CELLS

Periodic structures with that is designed to modify electromagnetic waves passing through them are broadly named electromagnetic band gap structures [32]. The dimensions of the periodic elements, the *unitcell*, are on the order of $\lambda/2$, in contrast to $\ll \lambda/2$ for metamaterials who often have similar or identical unitcells. Depending on the application, there is many different types of EBGs that goes under different terms, like photonic band gap (PBG) and FSS [32]. In this text, the general term EBG are used unless otherwise is noted.

This section aims to provide an overview of EBG. It is a wide topic, but it is attempted to give the necessary theory for a graduate student who isn't familiar with the material. It begins with a description of the basic EM properties that pertain to EBGs, followed by the working principle of an EBG material. The distinction between a metamaterial and an EBG material is then discussed. he section is concluded by an overview of the different flavors of unit cells.

It is stressed that much of the following text is reprinted from the author's previous work in the Autumn of 2020 [15].

2.4.1 *Electromagnetic Wave Parameters*

To introduce essential parameters, one may begin with the phasor form of the time-harmonic source free Maxwell's equations, given in equation (42) to (45),

$$\nabla \times \vec{H} = j\omega\epsilon\vec{E} \tag{42}$$

$$\nabla \times \vec{E} = -j\omega\mu\vec{H} \tag{43}$$

$$\nabla \cdot \vec{E} = 0 \tag{44}$$

$$\nabla \cdot \vec{H} = 0, \tag{45}$$

where $\omega = 2\pi f$ is the angular frequency of the wave, j is the imaginary unit.

By combining these equations, we obtain the second order partial differential wave equations for the electric and magnetic fields, called the homogeneous vector Helmholtz's equations [6]:

$$\nabla^2 \vec{E} + k^2 \vec{E} = 0 \tag{46}$$

$$\nabla^2 \vec{H} + k^2 \vec{H} = 0 \tag{47}$$

where

$$k = \omega\sqrt{\mu\epsilon} \tag{48}$$

is the *wavenumber*. This is a central parameter describing the spatial variation of the wave.

Generally, the wavenumber k is complex. The real part is related to the wavelength,

$$\mathrm{Re}\{k\} = \frac{2\pi}{\lambda}, \tag{49}$$

while the imaginary part describes the attenuation. These are called the phase and attenuation constant, respectively, often written as β and α, giving $k = \beta - j\alpha$ [16]. Moreover, when dealing with volumes, three wavenumbers are necessary and they form a vector of three elements, $\vec{k}$, describing EM propagation in all three dimensions. A singular wavenumber is in this case defined as $\left|\vec{k}\right|$.

The wavenumber is strongly tied to the *phase velocity*

$$v_p = \frac{\omega}{\beta}. \tag{50}$$

This is the speed at which a point of constant phase is propagating with respect to time.

The phase velocity is furthermore related to the *group velocity*,

$$v_g = \left(\frac{\partial\beta}{\partial\omega}\right)^{-1}. \tag{51}$$

This is the speed of energy transfer and is what one generally associates with the speed of a wave. It cannot be greater than the speed of light, though the phase velocity may be[17].

16 Some authors use instead of phase constant for β, but in this text the term *propagation constant* is reserved for $\gamma \triangleq \alpha + j\beta$ in accordance with transmission line theory.

17 Faster than light v_p may be illustrated by standing parallel to a shore and watching waves hitting the shoreline. If the wavefront is following the shore near orthogonally, it will look like the wave is traveling up towards you quite slowly. As the angle between the wavefront and shore increases, the apparent wave will travel towards you faster and faster until the wavefront becomes parallel with the shore. At this point, the whole wavefront will hit the shoreline at the same time, corresponding to infinite v_p - The phase only varies with time, not with space [31]. In all cases v_g was constant.

The *solution* to the Helmholtz's equations is a sum of exponentials in the general case, but only a single exponential if the wave is propagating in source free homogeneous media.

In the simplest case of a plane wave propagating in the z-direction, the electric field is described by

$$\begin{aligned}
\vec{E} &= E_x(z,t)\,\hat{\mathbf{z}} \\
E_x(z,t) &= \mathrm{Re}\{E_0 e^{-jkz} e^{j\omega t}\} \\
&= \mathrm{Re}\{E_0 e^{-\alpha z} e^{-j\beta z} e^{j\omega t}\} \\
&= \mathrm{Re}\left\{E_0 e^{-\alpha z} e^{-j\frac{2\pi}{\lambda}z} e^{j\omega t}\right\} \\
&= E_0 e^{-\alpha z}\cos\left(2\pi\left[ft - \frac{1}{\lambda}z\right]\right).
\end{aligned} \tag{52}$$

2.4.1.1 *Dispersion*

Loss and frequency dependent permittivity and permeability cause the wavenumber k to be complex and a nonlinearly function of frequency, called *dispersion relations*. The name comes from the fact that nonlinearity in $k(\omega)$ leads to different group velocities for different ω, as can be shown from (51). A narrow wave packet entering a dispersive media will be smothered out as it travels through it, i.e. dispersed. $\epsilon(\omega)$ is ordinarily much more dominant than $\mu(\omega)$ and have gotten the special the name *the dielectric function*.

Dispersion diagrams is a useful tool for visualizing the relation between k and ω. The primary axis is k – or β if the wavenumber is complex – and the secondary axis is ω, see figure 9 where the dispersion relation for ionized gas is plotted.

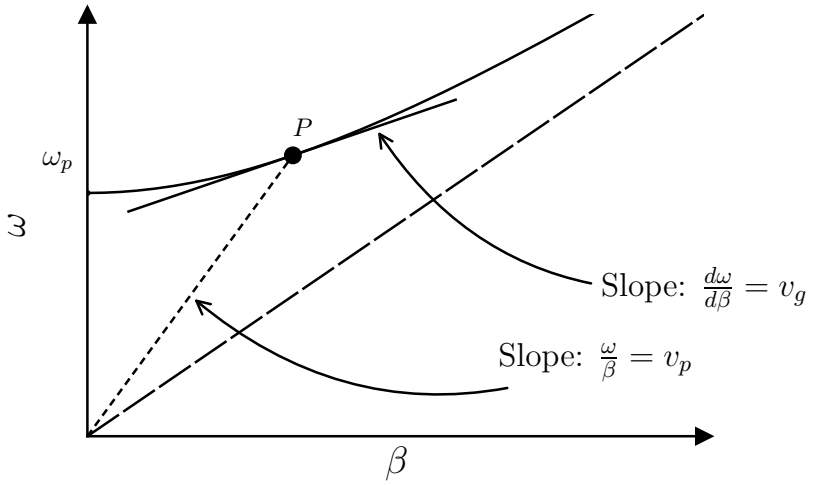

Figure 9: Illustration of dispersion diagram for a radio wave propagating through an ionized gas. The dashed diagonal line is the linear light line that waves in free space follows. Waves that characterized as curves above the light line are called fast waves, as in this case. Otherwise, they are called slow waves and are normally bound in a structure. The slope through any point P on the dispersion curve and its derivative gives the phase and group velocity, respectively. The ω_p point in the figure is called the plasmonic frequency and are characteristic of fast waves. The figure is based on ([6], p.377)

2.4.2 *Periodicity and Band Gaps*

In the discussion of metamaterials and electromagnetic band gap, periodicity is a central aspect. For EBGs, phenomena caused by periodicity are the main effects that are engineered and utilized. The theory of periodic structures is emphasized in this section because it is central to calculating the behavior of the EBG material. This stems from the fact that periodicity creates *boundary conditions* of Maxwell's Equations around a single unit cell, enabling the behavior of the whole EBG structure be found with only one unit cell.

We begin the discussion by creating the link between periodicity in space with periodicity in wavevector $\vec{k}$. Consider a 1D periodic structure, as illustrated in figure 10.

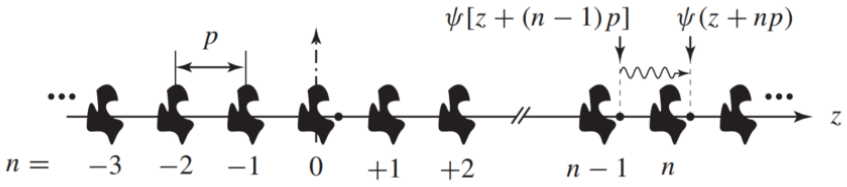

Figure 10: Illustration of a 1D periodic structure with periodicity p together with a propagating wave ψ at two points. In contrast to the text, this figure uses p instead of a for the period, and z instead of x for the position. Reproduced from ([5] p.106)

Assume that $\psi(x)$ is a propagating wave of arbitrary shape at point x in a loss-free a-periodic structure. It will differ from another point a away – $\psi(x+a)$ – only by a complex constant $C = e^{jk\cdot a}$ as only the phase has evolved. We can write this mathematically as

$$\frac{\psi(x+a)}{\psi(x)} = \frac{\psi(x+2a)}{\psi(x+a)} = \frac{\psi(x+na)}{\psi(x+(n-1)a)} = C \text{ for all } n. \tag{53}$$

Some manipulation yields the relation ([5], p.106)

$$\psi(x) = \psi(x+n\cdot a)e^{jkna}. \tag{54}$$

If multiplied by e^{-jkx}, it gives a new, *periodic* function

$$\xi(x) = e^{-jkx}\psi(x), \tag{55}$$

for any wavenumber k. Since it is periodic with a, we can express it by a Fourier series with Fourier expansion coefficients

$$\xi_{kn} = \frac{1}{2\pi}\int_{-\pi}^{\pi} \xi_{kn}(x)e^{-j(2\pi n/a)x}\ \mathrm{d}x\,, \tag{56}$$

assuming that the structure is infinite. This gives the Fourier expression for $\xi(x)$

$$\begin{aligned}\xi(x) &= e^{-jkx}\psi(x)\\ &= \sum_{n=-\infty}^{\infty} \xi_{kn}e^{j(2\pi n/a)x}.\end{aligned} \tag{57}$$

Solving for our wave function $\psi(x)$

$$\begin{aligned}\psi(x) &= \frac{\xi(x)}{e^{-jkx}}\\ &= \sum_{n=-\infty}^{\infty} \xi_{kn}e^{j(k+2\pi n/a)x}\\ &= \sum_{n=-\infty}^{\infty} \xi_{kn}e^{jk_n x},\end{aligned} \tag{58}$$

gives a central result: in any a-periodic system, the wavenumber k is *also periodic* with $2\pi/a$, $k_n = k + \frac{2\pi}{a}n$.

The wave function in expression (55) above, more commonly written as $\psi(x) = e^{jkx}\xi(x)$, is called a *Bloch function* in solid state physics. It describes that a wave propagating through a periodic structure may be represented as a plane wave e^{jkx} modulated by a periodic lattice function $\xi(x)$. Each $\psi(x)$ is called a Bloch wave and is an energy *eigenstate* of the lattice system [5].

2.4.2.1 *Bloch Floquet's Theorem and its Use in Full Wave Simulations*

In the more general case, the wave may travel in either x or $-x$ direction. The wave function (58) then becomes

$$\psi_k(x) = \sum_{n=-\infty}^{\infty} \xi_{kn}^{+} e^{jk_n x} + \sum_{n=-\infty}^{\infty} \xi_{kn}^{-} e^{-jk_n x} \tag{59}$$

and is called the *Bloch-Floquet's theorem* [5]. A wave in a periodic structure is therefore a superposition of an infinite number of plane waves $e^{jk_n x}$, called *space harmonics*. The wave for which $n = 0$, $k_0 = k$, is called the *fundamental*, while waves with $n < 0$ and $n > 0$ are called negative and positive space harmonics, respectively ([5], p.107). A consequence of the Bloch-Floquet's theorem is that no single space harmonic fulfills the boundary conditions on its own, only the sum does ([32], p. 67). This sum of any given k is called *mode*.

The Bloch-Floquet's theorem is utilized when numerical computer simulations are used to calculate the behavior of an EBG. In such electromagnetic (EM) calculations called *full wave simulations*, the lateral edges[18] are set to be *Floquet boundaries*, analogous to placing the unit cell within a figurative hall of mirrors. See Figure 11 below for an illustration.

18 The top and bottom edges of the unitcell is normally set to be free space via a perfect magnetic conductor (PMC)

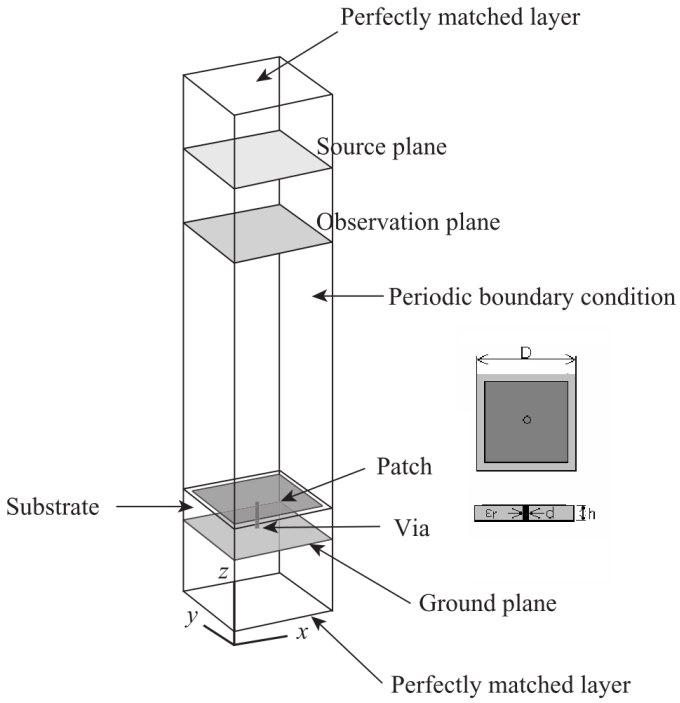

Figure 11: Illustration of simulation setup of a unit cell with Floquet boundary condition. The unitcell depicted is a so called *mush-room* cell, consisting of a metal patch connected to a ground plane with a via. It is shown in top-down and profile view on the inset on the right. A *source plane* excites plane waves towards the unit cell and a observation plane records the magnitude and phase of the reflected wave. Reproduced from ([32] p.8)

2.4.2.2 *Local Periodic Approximation*

The periodic analysis above assumes an infinite number cells in each direction, giving rise to the legitimate question if the theory still holds for finite arrays. As with other Fourier relationships, going from summing over an infinite number of elements to only a finite number does not ruin the effect. Rather, the previous definite points of k gets smeared out and broaden, lessening the effect.

This thesis, as with most other articles on transmitarrays, assumes that the *local periodic approximation* is true. This says that a single unitcell has the same properties as it would have in an infinite array. Time did unfortunately not permit to investigate how valid this approximation is.

2.4.3 *Limit on Layers*

There is an theoretical upper limit the maximum phase shift that can be achieved by a single transmitarray layer regardless of the element shape [2]. Most transmitarray designs therefore use multi layered unit cells, M-FSS, to get both high phase shift range and low loss. A brief summary of this theory is given here, but a full derivation is given in A.

Four assumptions are used to model an ideal single layer unit cell. The three first ones are: the S-matrix is symmetrical, reciprocal and lossless[2]. These assumptions results in the following relations:

$$S_{11} = S_{22} \qquad S_{21} = S_{21} \tag{60}$$

$$|S_{11}|^2 + |S_{11}|^2 = 1 \qquad |S_{11}|^2 + |S_{11}|^2 = 1 \tag{61}$$

$$S_{11}S_{12}^* + S_{21}S_{22}^* = 0. \tag{62}$$

The fourth assumption is that the higher order harmonics are negligible[2]. This gives the relation:

$$S_{21} = 1 + S_{11}. \tag{63}$$

Combining these equations gives the expression for S_{21}:

$$S_{21} = \cos(\angle S_{21})e^{j\angle S_{21}}. \tag{64}$$

The relation in (64) can be visualized by plotting the scattering parameter S_{21} in a polar diagram, see Figure 12. Other unitcells will also be plotted in this manner in the rest of this thesis.

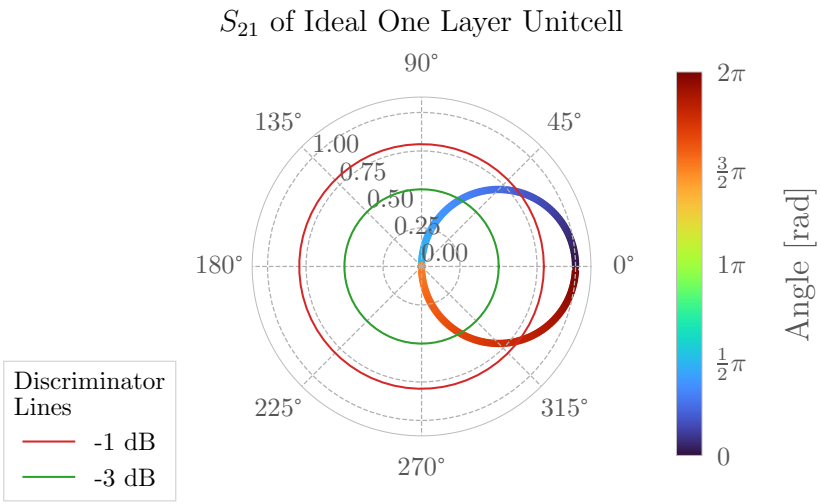

Figure 12: Polar plot of the scattering parameter S_{21} for an ideal single layer unitcell showing the maximum theoretical performance. The unitcell consists of only a metal layer without a substrate. The S_{21} curve is the thick colored curve where each color corresponds to a $\angle S_{21}$. The red and and green curves show the –1 dB and –3 dB magnitude limits. It is apparent that a single unitcells layer is only capable of covering a phase range of 54° when using the –1 dB loss limit. The plot's magnitude scale is linear.

It emphasized that the equation in (64) is independent of element shape, and the phase range illustrated by Figure 12 is the maximum range achievable. In order to cover a higher phase range, multiple layers must be used.

The theoretical analysis of the transmission coefficient of multiple layers is achieved by cascading the S-matrices for the individual layers. The expressions[2] for cascading two S-matrices a, b are:

$$S_{11} = \frac{S_{11}^b S_{12}^a S_{21}^a}{1 - S_{11}^b S_{22}^a} + S_{11}^a \tag{65}$$

$$S_{12} = S_{21} = \frac{S_{21}^a S_{21}^b}{1 - S_{11}^b S_{22}^a} \tag{66}$$

$$S_{22} = \frac{S_{22}^a S_{21}^b S_{12}^b}{1 - S_{11}^b S_{22}^a} + S_{22}^b \tag{67}$$

Between each of the metal layers of the unitcell, there are one or more substrates. These are also modeled with scatterings matrices and are cascaded with the other S-matrices of the unitcell's layers. The expression for lossless substrates of thickness t_s and relative permittivity ϵ_s is:

$$S_{11} = S_{22} = \Gamma \frac{1 - e^{-j2\beta t_s}}{1 - \Gamma^2 e^{-j2\beta t_s}} \tag{68}$$

$$S_{21} = S_{21} = \left(1 - \Gamma^2\right) \frac{e^{-j\beta t_s}}{1 - \Gamma^2 e^{-j2\beta t_s}} \tag{69}$$

$$\Gamma = \frac{1 - \sqrt{\epsilon_s}}{1 + \sqrt{\epsilon_s}} \tag{70}$$

$$\beta = \frac{2\pi\sqrt{\epsilon_s}}{\lambda} \tag{71}$$

where Γ holds for normal wave incidence.

It is convenient to combine β and t_s into a single number $\beta \cdot t_s$. This is the phase shift that the wave gets after propagating through the substrate. Adding a substrate of βt_s on a unitcell layer has one readily apparent effect of rotating the S_{21} curve by βt_s°.

Figure 13 shows four different unitcells with increasing number of layers. Each metal layer is identical, and there is a lossless substrate with $\beta t_s = 90^\circ$ between each metal layer.

Three important points are shown by Figure 13 below. Firstly, only the four layer unit cell is capable of achieving 360° phase range under the condition $|S_{21}| > -1$ dB. Secondly, the three layer unit cell maintain $S_{21} > -3$ dB for the whole 360° and almost does the same for $S_{21} > -1$ dB, except for a small region. Lastly, under the condition of using a lossless substrate, the magnitude of S_{21} increases for increasing number of unitcells. More layers than 4 can therefore be used to create arrays with lower loss.

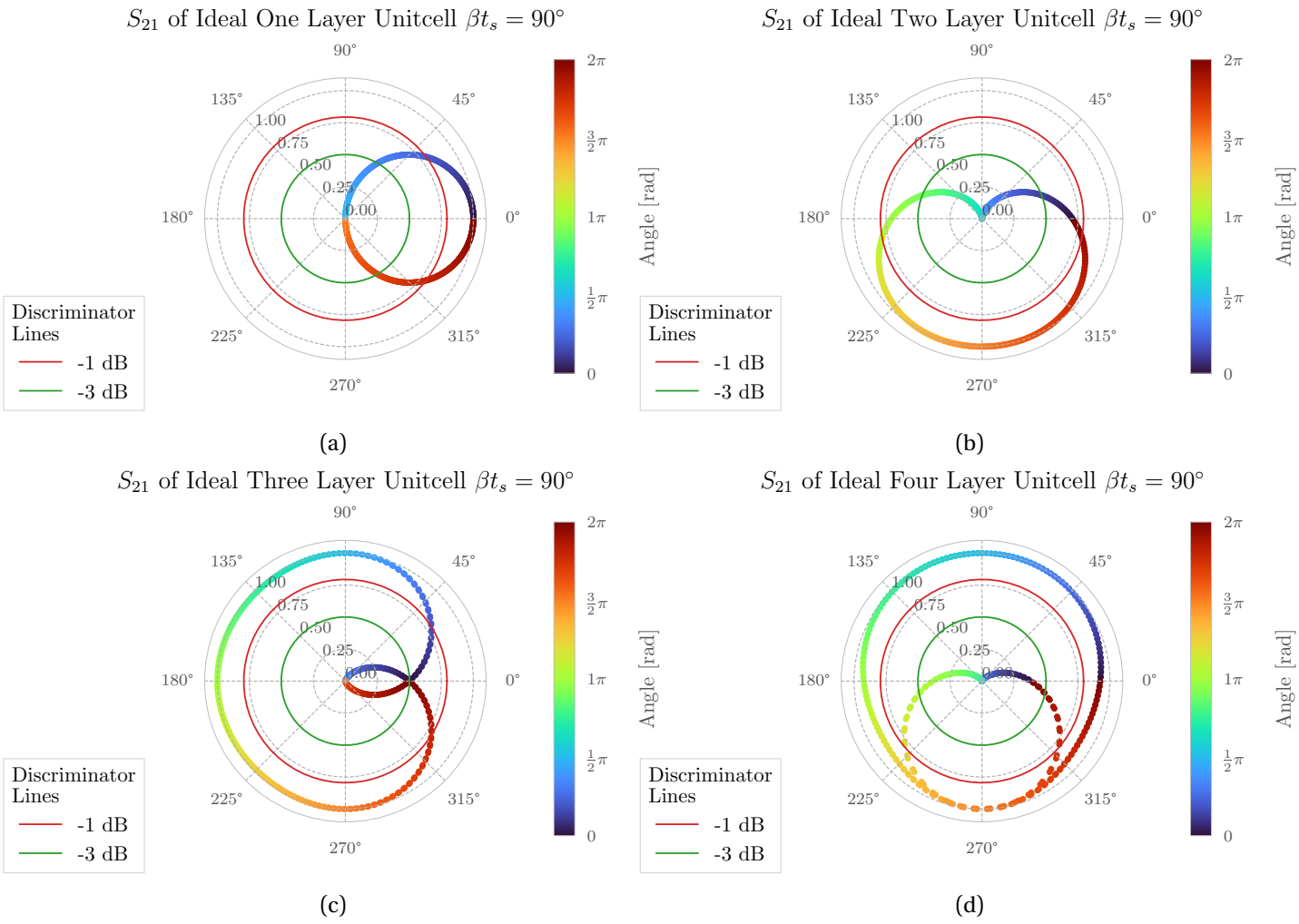

Figure 13: Polar plot of S_{21} for identical unitcells with (a) one, (b) two, (c) three and (d) four layers. All except the single layer unit cell have a lossless substrate between each metal layer with $\epsilon_s = 1$. These transmission coefficients are ideal and independent of element shape. It does not, however, show the maximum possible phase range since wider phase ranges can be achieved at the cost of decreased $|S_{21}|$.

Table 2 below summarizes the achievable phase ranges using identical unitcells for a given $|S_{21}|$ limit.

Table 1: Acheivable phase ranges for unitcells with 1 to 4 identical layers when $\beta t_s = 90°$ for a $|S_{21}|$ limit of –1 dB and –3 dB.

Number of Layers	**Phase Range**	
	–1 dB	**–3 dB**
1	74°	119°
2	157°	221°
3	293°	360°
4	360°	360°

Next, the effect of varying the substrate's electrical length βt_s is studied. The case of single and dual layer unitcell is used as representative cases. Their transmission coefficient is simulated for $\beta t_s \in [10°, 30°, 60°, 90°]$, see Figure 14 below. It is clear that $\beta t_s \neq 90°$ leads to a wider achievable phase range, but at a cost of decreased $|S_{21}|$.

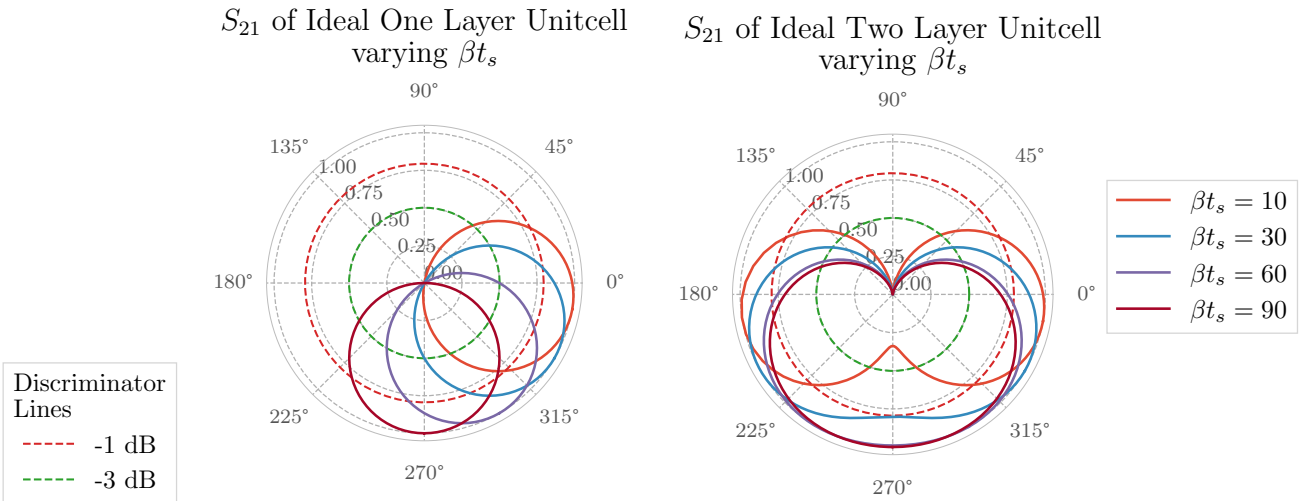

(a) (b)

Figure 14: Polar plot of S_{21} for identical unitcells with electrical length βt_s equal to 10° 30°, 60° and 90°. All have lossless substrates and $\epsilon_s = 1$. As the case of 10° makes apparent, the effect of changing βt_s rotates the circles in opposite directions. This leads to a wider phase coverage, but with less uniform $|S_{21}|$. It is noted that angles higher than 90° are not plotted since the response is symmetrical around 90° for the case of ideal unitcells. I.e. the case of 170° is identical to 10°.

Finally, the effect of ϵ_s is studied. In Figure 15, ϵ_s is varied while the electrical length of the substrate is kept constant. It shows that increasing the relative permittivity has two effects: squishing of the magnitude of the curves caused by increasing the reflection coefficient Γ through (70); and slightly increased phase coverage.

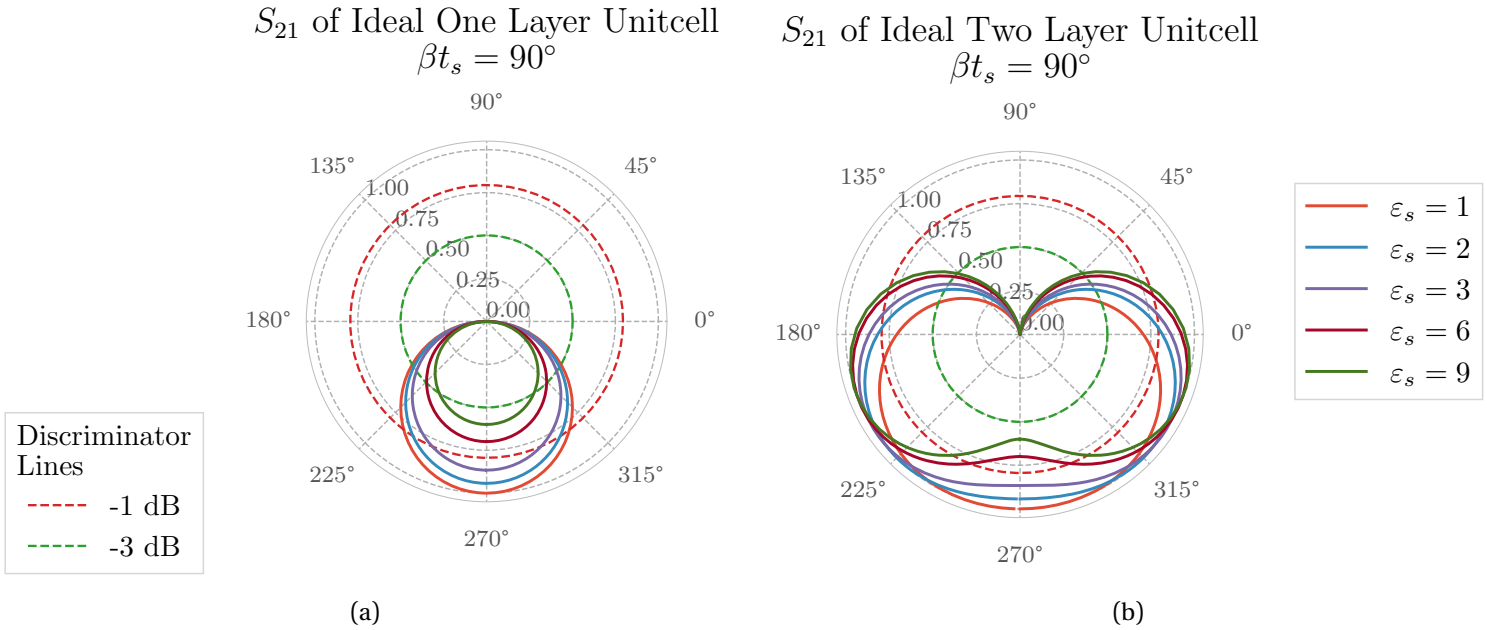

Figure 15: Polar plot of S_{21} for identical unitcells with varying substrate permittivity and constant electrical length.

2.5 PARTICLE SWARM OPTIMIZATION

Particle swarm optimization (PSO) is a modern numerical optimization technique based on the group behavior of organisms like a flock of birds or a swarm of ants. It aims to replicate the way these biological swarms search their environment to reach near optimum foraging behavior. In contrast to other numerical optimization techniques, the PSO algorithm depends only on the function values themselves and not their derivatives.

The algorithm is centered around a collection of points in the *design space*, $\vec{X}$, called *particles*. Each particle has two parameters: a *position* and a *velocity*. They wander around in the design space, evaluate an objective function $f\left(\vec{X}\right)$ and record their best position. This position is shared with the swarm and every particle adjusts their position and velocity accordingly.

The behavior of the swarm is based on three factors[25]:

1. Cohesions – stick together.
2. Separation – don't come too close.
3. Alignment – follow the general heading of the flock.

2.5.1 *Functional Description*

Maximize the objective function $f\left(\vec{X}\right)$ subject to

$$\vec{X}^{(l)} \leq \vec{X} \leq \vec{X}^{(u)}$$

where $\vec{X}^{(l)}, \vec{X}^{(u)}$ is the lower and upper bound, respectively.

1. Assume a swarm size of $N \cong 20$ to 30.
2. Generate an initial population randomly. Let the jth particle position be $\vec{x}_j(i)$ for iteration i. All velocities are assumed to be initially zero.
3. Evaluate the objective function for each particle.

4. In the ith iteration, find the following two important parameters used by a typical particle j:

   a) The historical best value $\vec{x}_j$, denoted as $\vec{P}_{\text{best},j}$.

   b) Find the velocity as follows:

$$\begin{aligned}\vec{V}_j(i) = \vec{V}_j(i-1) &\\ + c_1 r_1 \left[\vec{P}_{\text{best},j} - \vec{X}_j(i-1)\right] &\\ + c_2 r_2 \left[\vec{G}_{\text{best},j} - \vec{X}_j(i-1)\right], \quad j = 1, 2, \ldots, N &\end{aligned}$$

   where c_1 and c_2 are the individual and group learning rates. They denote the relative importance of position of the particle relative to the position of the swarm. The parameters r_1 and r_2 are uniformly distributed random numbers in the range 0 to 1.

   c_1 and c_2 are assumed to be 2 so that cr ensure that the particles overly the target about half the time

   c) Find the position or coordinate of the j particle in the ith iteration as

$$\vec{X}_j(i) = \vec{X}_j(i-1) + \vec{V}_j$$

   d) Evaluate the objective function

5. Check the convergence of the current solution. If the positions of all particles converge to the same set of values, the method is assumed to have converged.

   If the convergence criterion is not satisfied, goto step 4.

3

DESIGN AND IMPLEMENTATION

Four design elements is central to the design of the transmitarray and these will be discussed in this chapter. These are: the feed antenna (p. 39), the surface layout (p. 43), the unitcell selection (p. 47), and the phase distribution of the array (p. 54). In addition, a final section (p. 62) shows the physical construction of resulting transmitarray.

3.1 FEED

3.1.1 *Feed Selection*

The choice of what type of antenna that should be used to illuminate the transmitarray would in practice be determined by the overall system requirements. As the goal of this thesis is to evaluate the lens surface itself rather than aiming at any specific real world application, the feed is chosen to be a horn antenna. This type of antenna is easy to set up, has a low sidelobe levels and exhibit low cross-polarization levels. A closer description of this type of antenna is given in Section 2.3.4 in the Theory chapter.

The center frequency of the system, and therefore the frequency of the feed, is chosen on the basis of two criteria: maximizing the directivity of the array and the availability of suitable horn antennas in the inventory. The first criterion necessitates/prefer/suggests/advocate high frequencies[1] since the number of $\lambda/2$ unitcells inside a given area increases and maximum directivity is proportional with the number of unitcells.

The selected feed is a Sivers 8 GHz to 12.4 GHz Horn having a flare length of 131 mm and an aperture of 50 mm $\times$ 73.6 mm, see Figure 16 and Figure 17. This was the smallest available horn in the 10 Ghz region, meaning that the farfield distance, and therefore the shortest focus distance, is shorter.

1 Higher frequencies does also increase losses in the substrates, but this factor was challenging to account for as no material data was available for the GHz-range for the FR4-substrates in question.

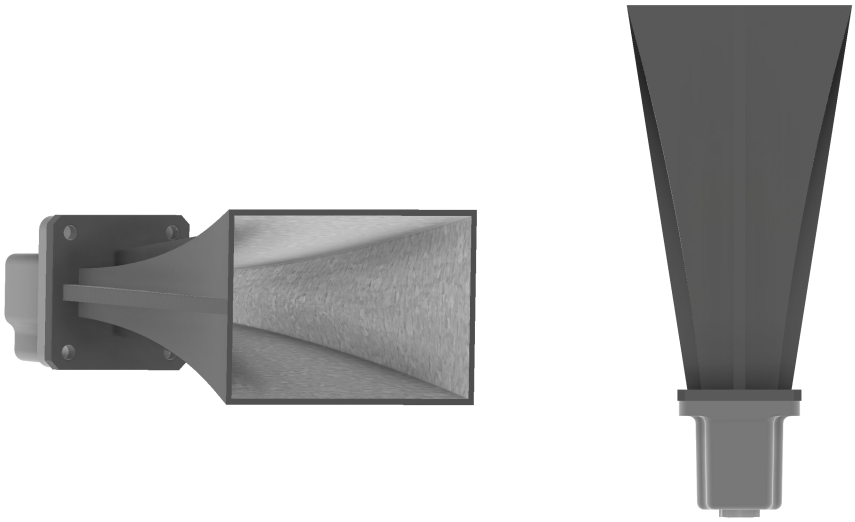

(a) (b)

Figure 16: Front (a) and bottom (b) view of a 3D model of the selected horn antenna that is used as a feed to the transmitarray. The model was created by taking measurements of the physical horn and was not supplied by the horn manufacturer. Also seen in these images is the gray coaxial-to-waveguide transition.

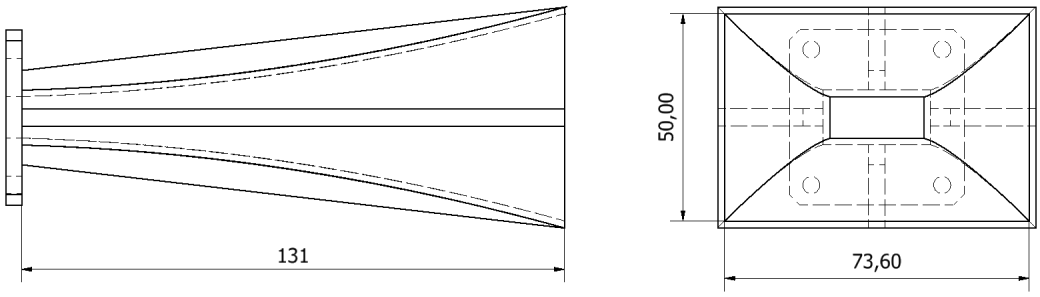

Figure 17: Technical drawing of the feed horn depicted in Figure 16 with all measurements in millimeters.

3.1.2 *Feed Characterization*

The feed horn is drawn in CAD[2] and simulated in EM-software[3] in order to characterize it. Of interest is the position of the phase center and the radiation pattern. The former is used to set the focus distance, and the latter is imported into the transmitarray design program. These are shown in Figure 18 and 19, respectively.

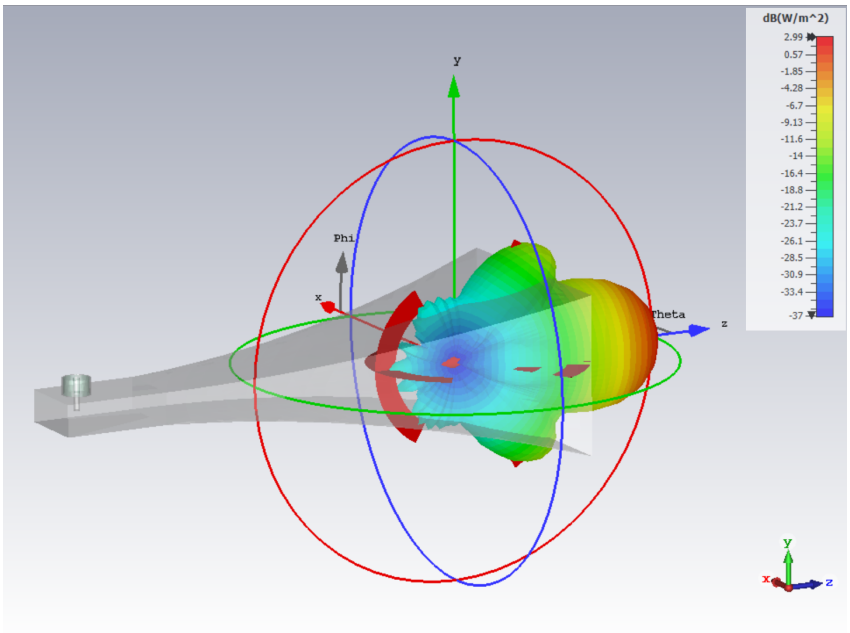

Figure 18: View of the horn structure used in EM-simulation and simulation result at 12 GHz. The colorful protrusion is the farfield power pattern centered at the phase center, which is the flat red arcs. The horn structure is shown as transparent with the coaxial transition to the rear. The structure is somewhat different from that shown in Figure 16 as only the inner surface is used in the simulation.

2 Computer Aided Design. Generic term for 3D modeling software.
3 CST Studio

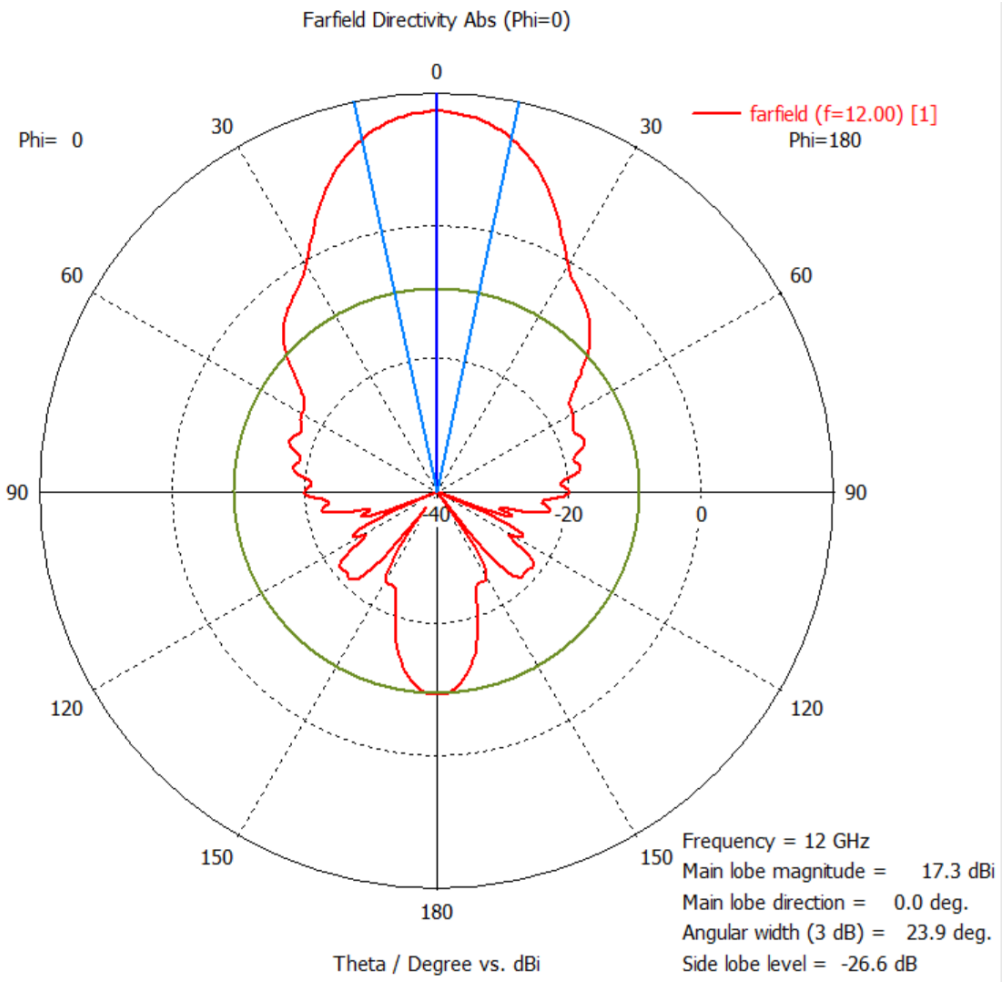

Figure 19: Polar plot of the farfield pattern of the horn antenna with a constant $\phi = 0$ at 12 GHz. It shows a broad main lobe that has a 3 dB width of 23.9° with a maximum directivity of 17.3 dBi. The simulation result has a pronounced backlobe which is partly due to the structure being simulated as an infinitesimal thin surface with perfect conductivity, leading to of the excessive current flow on the outside of the horn.

3.2 SURFACE

There are three parameters that needs to be defined for the transmitarray. They are: the overall shape, the diameter and the focus distance. The overall shape could in theory be arbitrary as long as the periodic approximation is satisfied. Since a circular perimeter is uncomplicated to design and the farfield of the feed is approximately circular, this shape is chosen for the design in this text. An example of such a circular layout is shown in Figure 20.

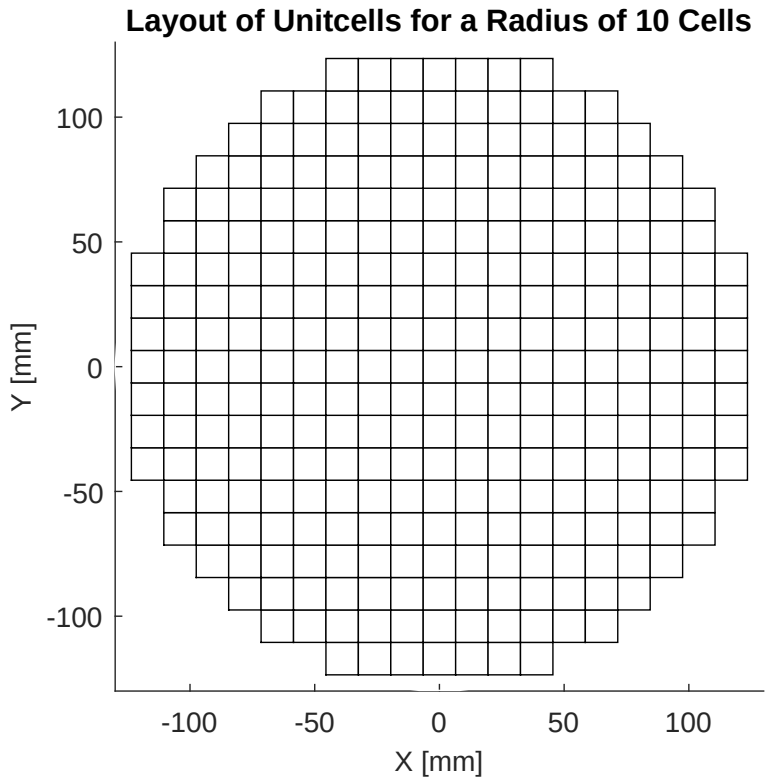

Figure 20: Layout of unit cells in a circular pattern. The diameter of the surface is 20 unitcells, each having a side length of 13 mm.

3.2.1 *Focus Distance*

The driving guideline for choosing the focus distance for this thesis is achieving a compact antenna design. This corresponds to a short focus distance. The limiting factor for how short this distance can be is twofold: placing the lens outside of the nearfield and avoiding coupling effects between the horn and array surface. It was chosen to be 400 mm.

The farfield distance is first estimated based on the horn aperture and then checked with simulation software. An approximate farfield distance is calculated to be 430 mm from equation (4) with a aperture opening of 73.6 mm at 12 GHz. As the transition from nearfield to farfield is gradual, an EM-simulation software[4] is used to calculate the magnitude of the radial component at 300 mm and 400 mm. These were found to be –25 dB and –30 dB respectively.

The possible coupling effects are harder to estimate because the reflection from the transmitarray are unknown at this stage and full system simulations takes a long time. The latter could be used to estimate the effects of different possible reflection values for the surface and judged whether these effects were substantial or not. Instead, the farfield distance is used as the limiting factor and the focus distance set at 400 mm.

3.2.2 *Surface Diameter*

The transmitarray will be more directive and capture a larger portion of the energy from the feed as the diameter increases. At the same time, one would want to keep the lens as small as possible from a practical standpoint. To determine a possible optimum diameter, a transmitarray with ideal elements is simulated[5] while its size is adjusted. The result is seen in figures Figure 21, Figure 22 and Figure 23.

4 CST Studio
5 The transmitarray was illuminated with field from the simulated horn feed from Section 3.1.

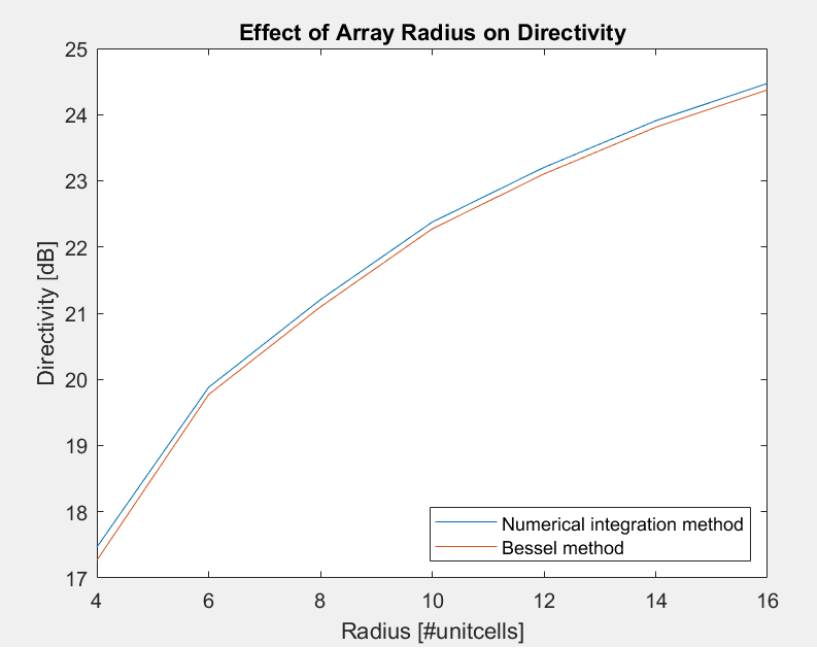

Figure 21: Plot of directivity of the transmitarray at a focus distance of 400 mm for increasing transmitarray radius. The unitcells are modeled as ideal, and the simulated feed radiation pattern is used. The results from two different numerical methods, numerical integration and the Bessel method described in Section 2.3, are shown together.

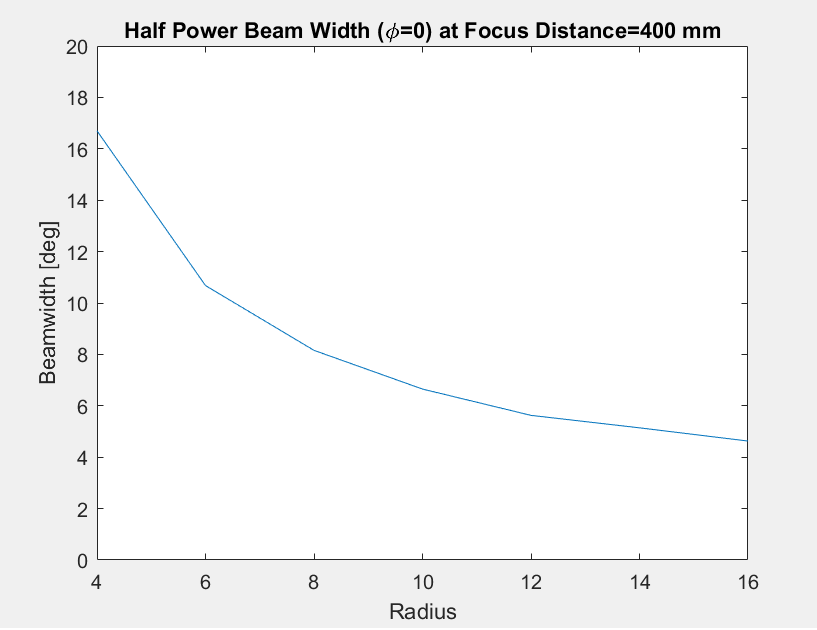

Figure 22: Plot of the half power beam width of the main lobe in degrees at a focus distance of 400 mm for increasing transmitarray radius, given in number of unitcells. It is seen that the beam width starts leveling off as the radius is increasing beyond 10 unitcells.The HPBW is measured in the θ-plane at $\phi = 0°$, the unitcells are modeled as ideal, and the simulated feed radiation pattern is used.

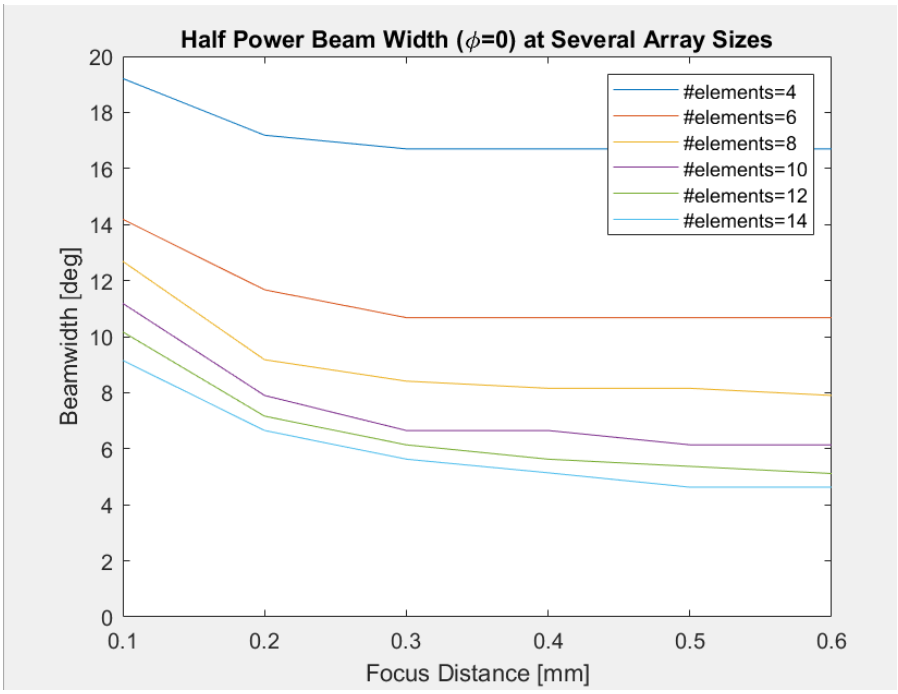

Figure 23: Plot of the half power beam width of the main lobe in degrees for increasing focus distance for several different transmitarray radii. It is seen that the beamwidth is only weakly affected by the focus distance. The HPBW is measured in the θ-plane at $\phi = 0°$, the unitcells are modeled as ideal, and the simulated feed radiation pattern is used.

There are several things to note from these figures. Firstly, the directivity is monotonically increasing with array diameter and has no marked leveling off within the simulated interval. Secondly, the HPBW is leveling off after the radius increases beyond approximately 9 to 10 unitcells. Lastly, the choice of focus distance has little effect on HPBW. Based on this, the transmitarray radius is chosen to be 10 unitcells.

3.3 UNITCELL SELECTION

The structure of the unitcell consists of the unitcell element, being the metal layer, and the substrate on which this metal layer is adhered to. The of selection of the element and substrate are discussed in this section.

As will be detailed in the following paragraphs, the unitcell is chosen to be a three layer M-FSS double square loop unitcell with a period of $a_x = a_y = \lambda/2 = 12.49$ mm with a 1 mm FR4 substrate and 10.2 mm air gap between each layer. It achieves a 54° phase range under the −1 dB criterion, and 183° under the −3 dB criterion.

3.3.1 *Substrate*

A 1 mm FR4 glass fiber substrate with permittivity $\varepsilon = 4$ and loss tangent of $\tan\delta = 0.012$ at 10 GHz is used as substrate for the unit cell. Ideally an RF-substrate with low loss and guaranteed permittivity should be used. This is not employed in this thesis primarily because of prohibitive cost for the required dimensions, but also because such substrates generally have low stiffness. By the same reason as the latter, 1 mm is used rather than 0.8 mm which was also available from the supplier[6].

An air gap of 10 mm is placed between subsequent layers in order to get a $\beta t_s = 90°$. This angle achieves the highest $|S_{21}|$ as was shown in Section 2.4.3. The substrate thickness represents the combined FR4 and air sandwich, requiring that S-matrix cascading with (65)-(65) is used to find and solve for the necessary thickness of air.

3.3.2 *Element Type Selection*

The choice of unitcell elements for this thesis is based on two factors: it is desired that the design should be simple, and no novel element type is to be developed. Higher performance can be attained with dissimilar cell elements and varying the substrate thickness or permittivity [3]. This does however increase development time and manufacturing cost. Only extant unit cell types are investigated since previous works have showed that these elements come close to the theoretical limit given in Section 2.4.3[3].

6 After receiving the FR4 substrate, it was found that 1 mm is far than stiff enough such that 0.8 mm would most likely also work.

Two guidelines are followed when narrowing down an appropriate unit cell type for the transmitarray: it must have high transmission and preferably be polarization independent. The former rules out patch-like elements, while the latter favors loop elements and N-pole unitcells with high N.

Two from the first group and two from the latter group is investigated: single and double square loop cell; and simple cross and Jerusalem cross cell. Illustrations of these are shown in Figure 24.

It was discovered that using unitcells that includes the intended substrate gave a better basis for comparison as opposed to only using the metal layer. Simulation results for the latter are included in Appendix B for those interested.

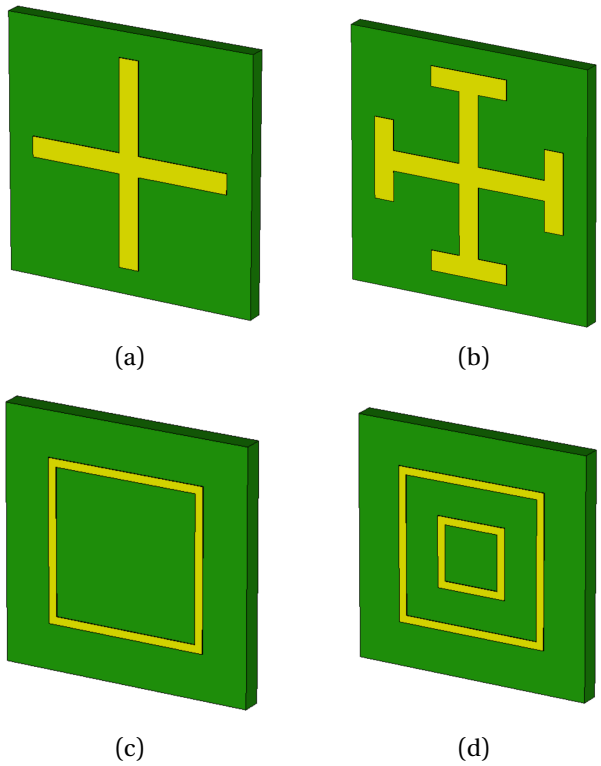

Figure 24: Illustration of the four different types of unit cells used that were investigated. These are: a) simple cross, b) Jerusalem cross, c) single square cell, and d) double square cell. Each cell has edge lengths of $a_x = a_y = \lambda/2 = 12.49\,\text{GHz}$. The substrate is 1 mm thick and the copper layer is 35 µm thick. The trace lengths are 1 mm for the crosses and 0.5 mm for the square loops, but has little effect on the S_{21} parameter. The reason for this discrepancy is that the inner edges of the loops coalesce to quickly for small loop diameters if the trace width was 1 mm.

The crosses are investigated because they have 90° rotational symmetry and it is possible to scale them down reasonably small before the metal edges coalesce. N-pole unitcells with higher order coalesces more rapidly and is therefore not used. The stubs at the ends of the Jerusalem cross adds capacitance and should lower the resonance frequency [20]. The S-parameter simulations of these unitcells are shown in Figure 25.

The loops are the most interesting candidate since they ideally have full rotational symmetry. Double loop designs are the most prevalent in literature since the second loops adds both capacitance and inductance, and it is reported to be the most wideband element [.] Square loops was chosen instead of circles simply because it requires fewer mesh-cells in the EM-simulation for one of the used solvers. The S-parameter simulations of these unitcells are shown in Figure 26.

There are several of important points that the simulations plots show. Firstly, the simple cross has the highest resonance at 10 mm while the double square loop has the lowest. Secondly, the addition of stubs on the Jerusalem cross did lower the dimensions at which the cross resonates, in addition to making the S_{21} circle more symmetric.

Third, the single and double square loop appear to cover roughly the equal phase ranges. Lastly, introduction of the second loop lowers the width at which resonance occurs and creates a second resonance on the upper end of the loop width.

3.3.3 *Double Loop Unit Cell*

The double square loop unit cell is chosen for this design, even though both the simple cross element and single square loop element appear to have similar characteristics. The primary reason for this decision is the reports from other authors that the loop element has the highest rotational invariance [20] and provides the wides band width [3]. Unfortunately, time constraints prevented a thorough verification of these claims.

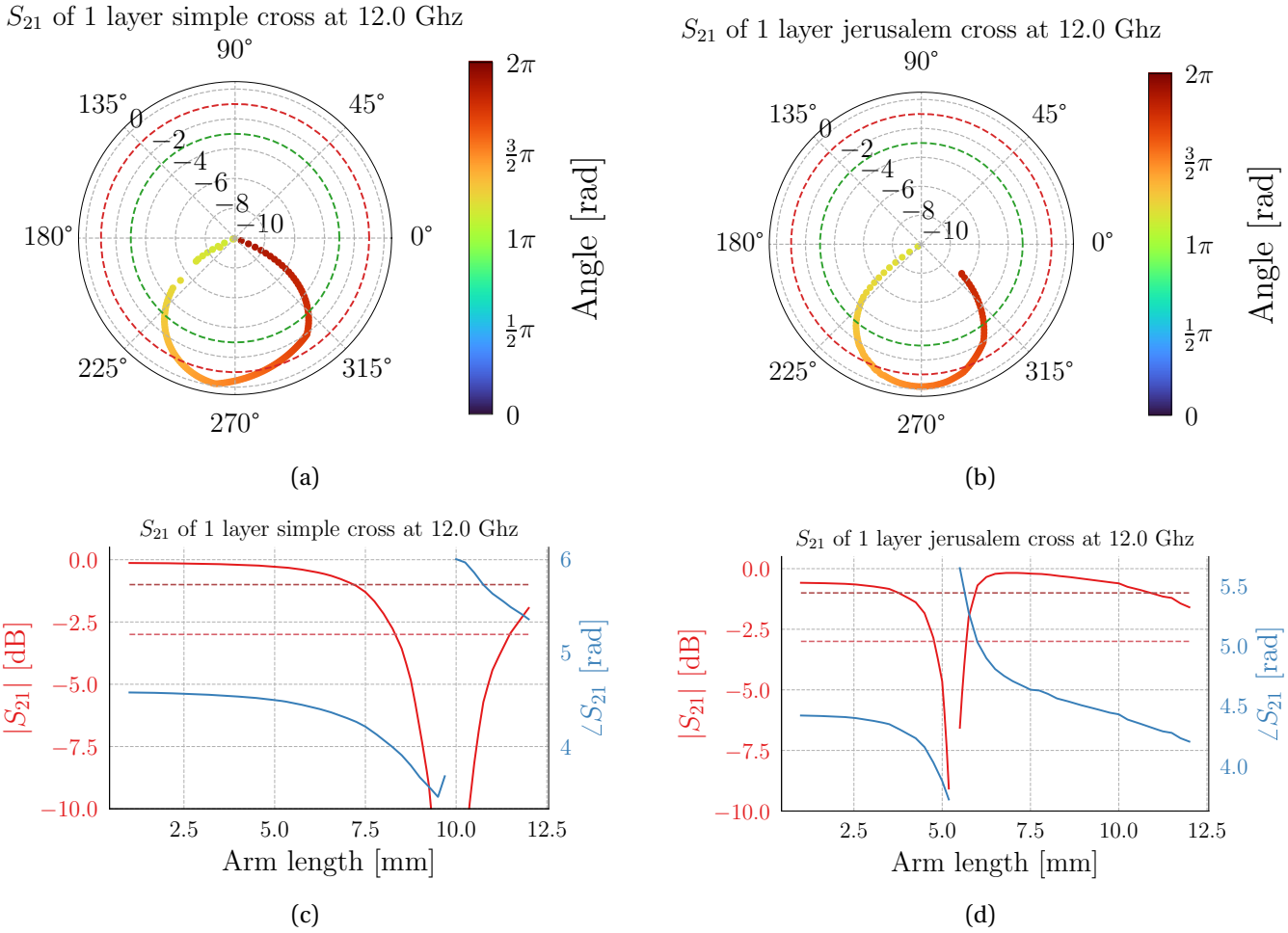

Figure 25: Full wave simulation results of the transmission coefficient S_{21} for simple cross and Jerusalem cross unit cells. The structure of the cells are seen in Figure 24 above. The stub length of the Jerusalem cross is $0.5 \cdot$ arm length. The the magnitude is given in dB for the polar and line plots. The dotted lines in all the graphs are the –1 dB and –3 dB magnitude lines. All unit cells have the same periodicity of $a_x = a_y = \lambda/2 = 12.49$ GHz and have Floquet ports on each lateral side of the unit cell. All simulations were done with inclination angle of $\theta = 90°$. The simulated substrate is a 1 mm thick FR4 with $\varepsilon = 4$ and $\tan\delta = 0.012$.

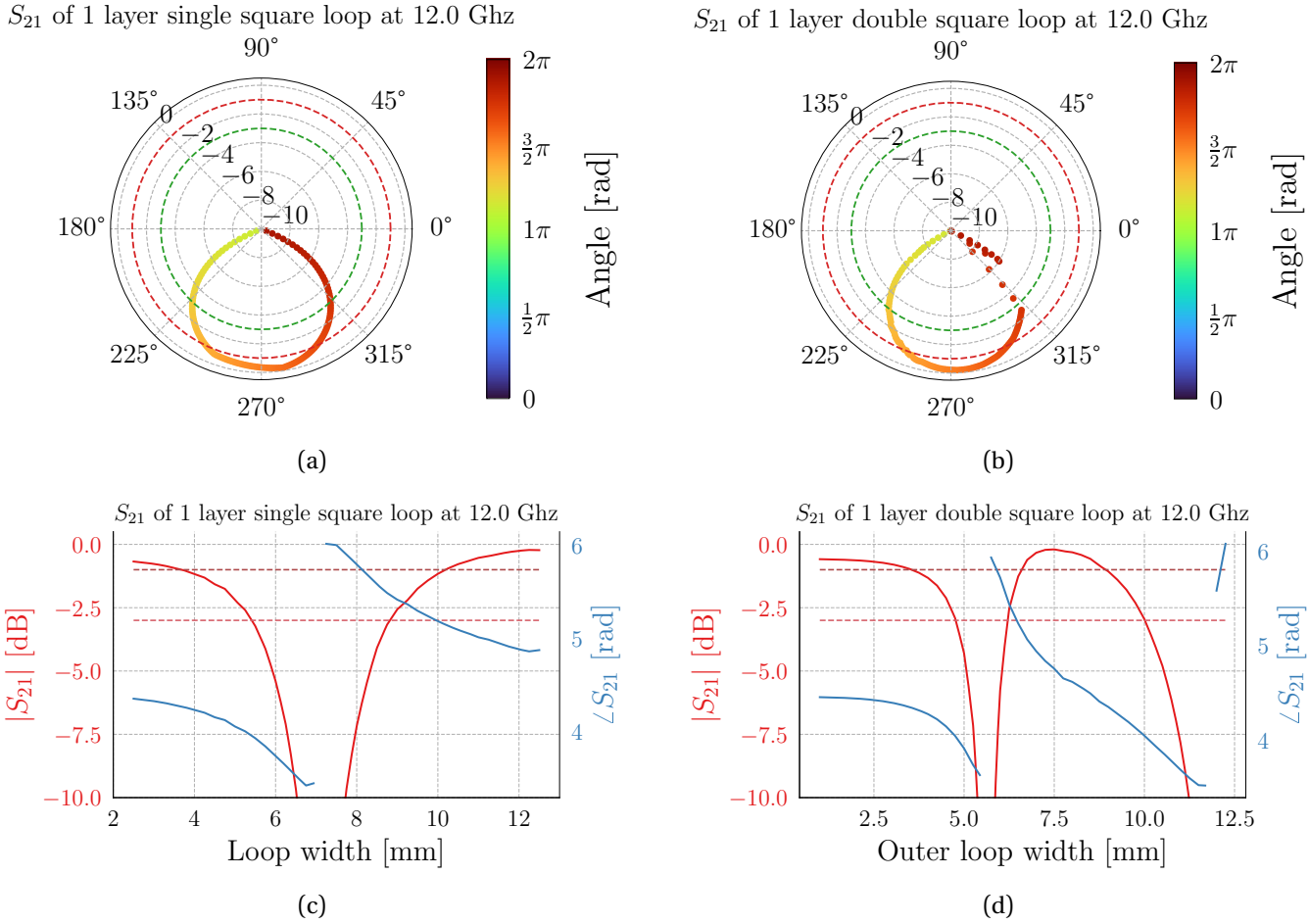

Figure 26: Full wave simulation results of the transmission coefficient S_{21} for single square loop and double square loop unit cells. For the double square loop unit cell, the separation between the inner and outer loops is $0.22 \cdot$ width of the outer loop. The structure of the cells are seen in Figure 24 above. The the magnitude is given in dB for the polar and line plots. The dotted lines in all the graphs are the –1 dB and –3 dB magnitude lines. All unit cells have the same periodicity of $a_x = a_y = \lambda/2 = 12.49$ GHz and have Floquet ports on each lateral side of the unit cell. All simulations were done with inclination angle of $\theta = 90°$. The simulated substrate is a 1 mm thick FR4 with $\varepsilon = 4$ and $\tan\delta = 0.012$.

3.3.4 *Number of Layers*

The transmitarrays discussed in this thesis uses 3 layers. As explained in Section 2.4.3, this makes it possible to achieve 293° phase range under the 1 dB loss criterion, as opposed to 157° to 360° phase range for 2 and 4 layers, respectively.

More layers than three is not chosen because of two reasons. Firstly, the transmitarray design will use FR4 as substrate and it was a high degree of uncertainty how lossy the substrate would be. A high number of layers is suspected to have greater dielectric loss than the additions of layer would be able to compensate[7]. Secondly, numerous simulations with truncated phase ranges showed that the loss in directivity between 4 and 3 layers was rather small[8].

3.3.5 *Final Unit Cell Simulation*

The final simulated transmission coefficient of the full three layer double square loop unit cell is shown in Figure 27 below. The −1 dB phase range is 54° and the −3 dB phase range is 183°. This is considerably lower than an ideal unitcell, but since radiation analysis (section Section 3.4) showed that this still is enough for demonstrating focusing and beam shaping, no further unit cell changes was done.

7 It was however not done good enough simulations to support or reject this speculation.
8 These simulation results was unfortunately not included in this paper.

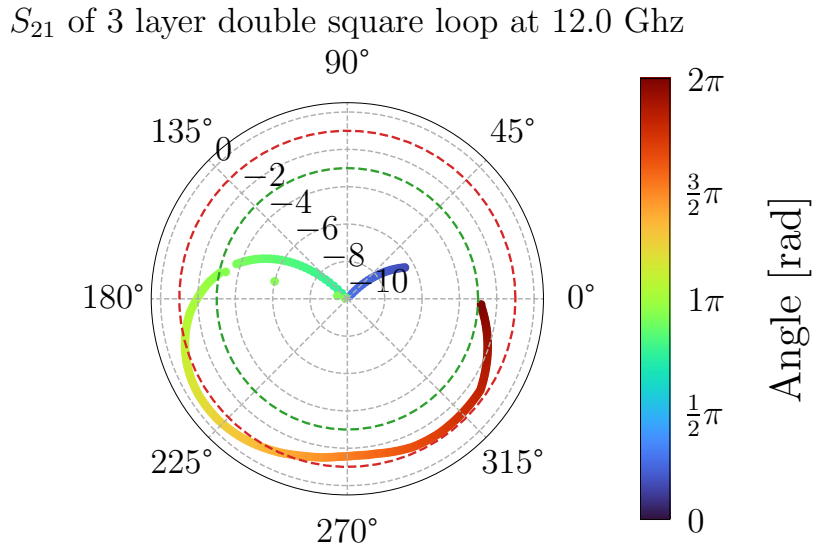

(a)

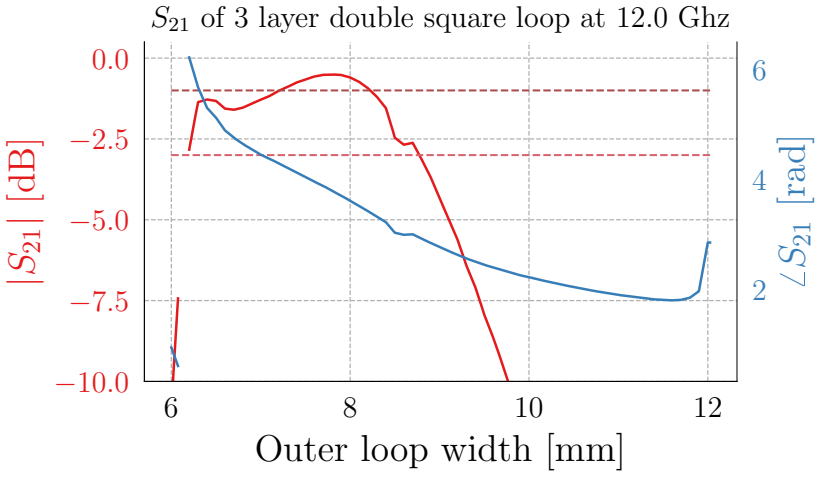

(b)

Figure 27: Full wave simulation results of the transmission coefficient S_{21} for the M-FSS unit cell used in the design. The element is a double square loop with a 2.5 mm separation between the inner and outer loops. The simulated substrate is a 1 mm thick FR4 with $\varepsilon = 4$ and $\tan\delta = 0.012$. Furthermore, the air gaps between the layers are 10 mm, and the metal is 35 µm lossy copper. The the magnitude is given in dB for the polar and line plots. The dotted lines in all the graphs are the –1 dB and –3 dB magnitude lines. All simulations were done with inclination angle of $\theta = 90°$.

3.4 PHASE DISTRIBUTION

3.4.1 *Phase Distribution 1.*

The initial phase distribution for the first surface where $\psi_0 = 0$ is shown in Figure 28.

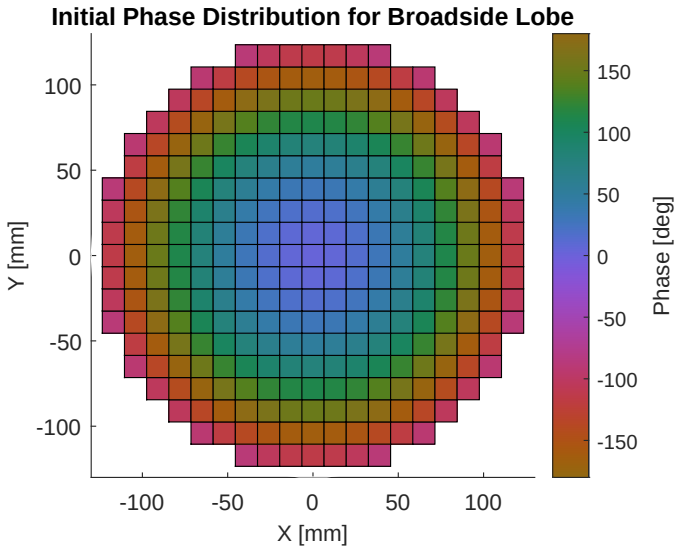

Figure 28: Phase distribution of the transmitarray for generating a broadside radiation pattern. In this distribution, the phase constant $\psi_0 = 0$. The values listed along the color bar is in degrees.

The next step is determining the value of the phase constant ϕ_0. Changing this parameter does not change the radiation pattern as this depends on the phase differences between unitcells, but it does change the distribution of the unitcell dimensions. This makes it possible to arrange the elements so that the overall transmission loss is minimized. place cells that has the lowest loss in the center where the feed illumination is the strongest, thereby minimizing the overall loss.

Other transmitarrays chooses ϕ_0 such that the least lossy elements in the center and the most lossy elements at the rim[3]. Since center is illuminated the strongest[9], this should intuitively result in the smallest overall loss. Tests done in this thesis did however show that this isn't always the case. Below in Figure 29 is a visual representation of how total element losses of the transmitarray is calculated.

9 For center feed arrays.

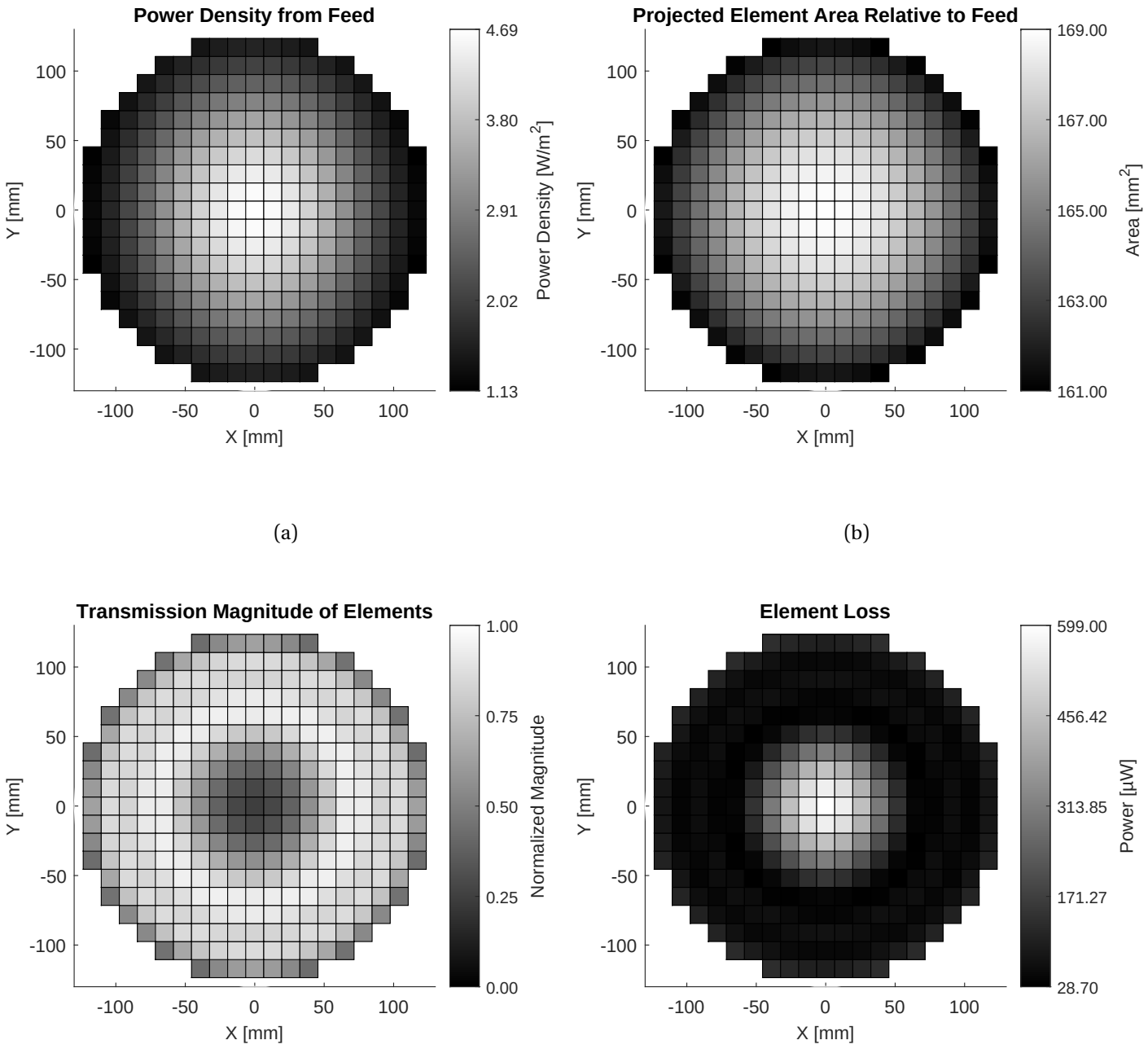

Figure 29: Visual illustration of how element losses are calculated. Subfigure (a) shows the power density at the surface of the array when it is illuminated by the horn feed at a distance of 400 mm. This density is multiplied by the projected element area as seen from the feed shown in (b). Here, the feed is modeled as a point source. The resulting power distribution is multiplied by transmission loss, $1 - |S_{21}|$, to get the element losses shown in (d). All the element losses are summed to get the total transmission loss of the surface. The $|S_{21}|$ of the elements stems from full wave simulations. The reflection magnitude is also included $(1 - S_{21})$ as a loss.

Directivity and loss calculations using radiation analysis is done for all possible phase offsets in order to determine the optimum value of ψ_0. The result are shown in Figure 30. It is apparent that peak directivity and minimum in overall loss are not achieved for the same phase offset, even though they are close.

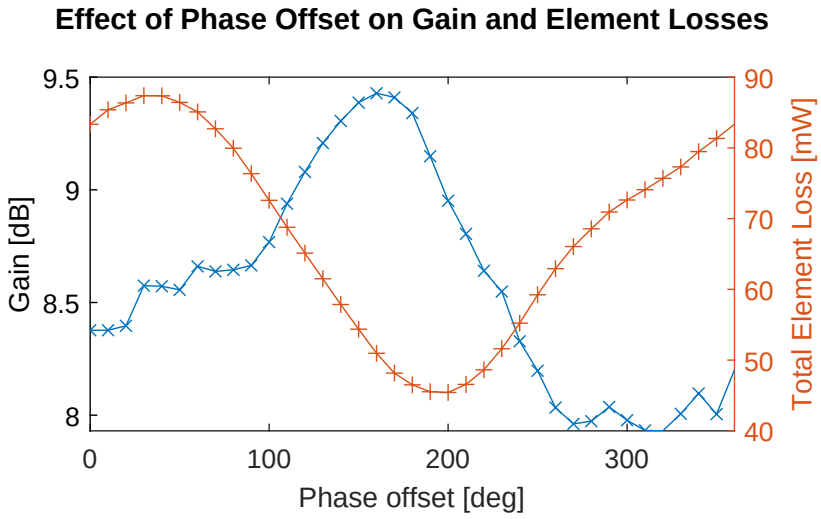

Figure 30: Radiation analysis of directivity and element losses as the phase offset ψ_0 is changed. The directivity is the blue curve having cross point markers, while the element losses are the red trace having + point markers. The total power sent into the feed is 0.5 W. It is seen that even though the values of directivity and loss are negatively correlated, their extrema are not collocated. The $|S_{21}|$ of the elements stems from full wave simulations.

A possible explanation for why the extrema of directivity and loss have different values of ψ_0 is truncation of elements. As mentioned in Section 2.4.3, a three layer transmitarray is not sufficient to cover the whole 0 – 360 phase range. Elements that require unsupported phase values are truncated to the closest supported phase. Figure 31 shows the number of truncated elements and the sum of all the truncated phase errors. It seems to support the hypothesis that truncation of elements has a significant impact on the optimum phase offset.

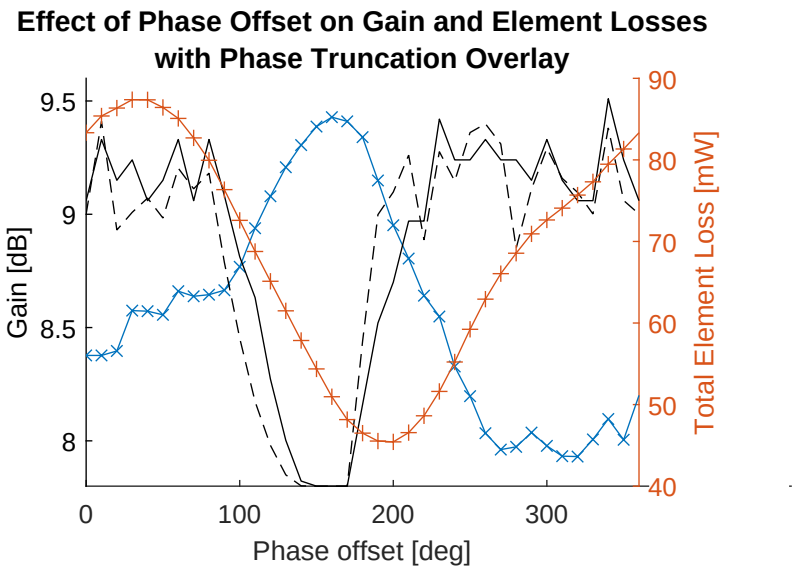

Figure 31: Extension of Figure 30 with element truncation added as black curves. The number of truncation elements is the solid black curve and the truncation error as a dashed curve. The latter is calculated as $\sum |\Delta\phi|$ where $\Delta\phi$ is the difference between ideal and truncated phase value. No y-axis is provides for these curves. The number of truncated elements range between 0 and 64.

From the above figures, peak directivity is achieved at $\phi_0 = 155°$. The final phase and magnitude distribution for the array is given in Figure 32. In addition, the resulting phase and magnitude distributions of the feed and the surface are given in Figure 33. The uniform phase distribution shows that the wave is collimated after leaving the transmitarray.

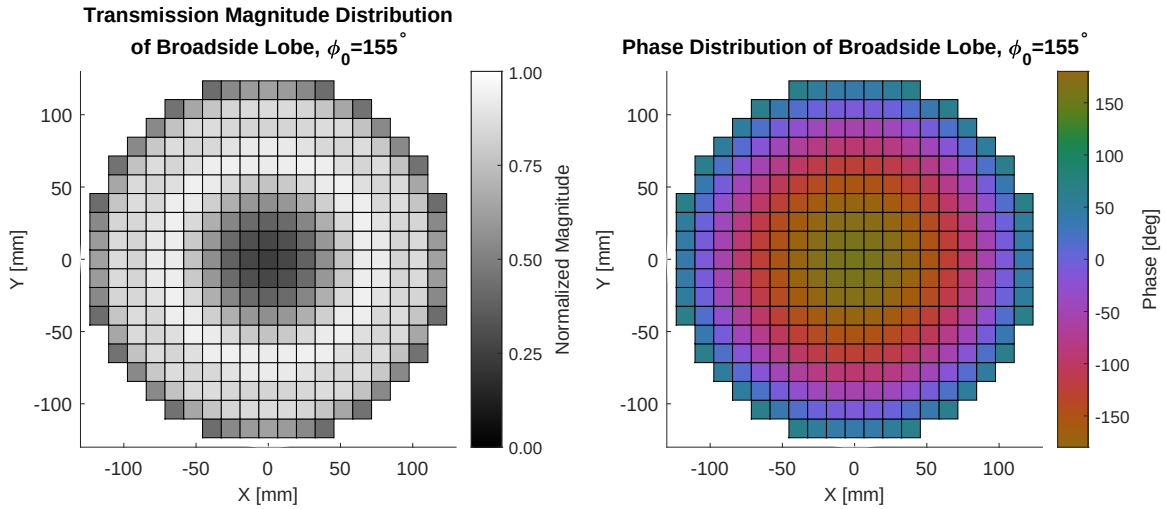

(a) (b)

Figure 32: (a) Magnitude and (b) phase distribution of S_{21} of each unit-cell in the transmitarray for a constant phase offset $\psi_0 = 155°$.

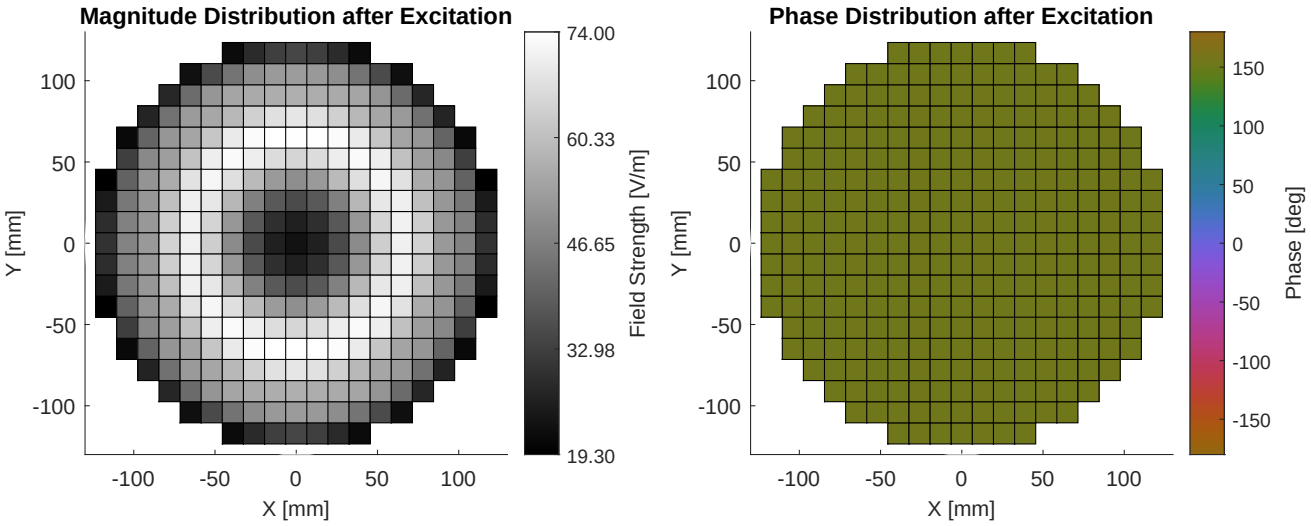

(a) (b)

Figure 33: (a) Magnitude and (b) phase distribution of the combined feed + surface system for a constant phase offset $\psi_0 = 155°$. As is seen from the uniform phase distribution, the wave exiting the transmitarray is collimated.

3.4.2 *Phase Distribution 2.*

The second phase distribution is found with numerical particle swarm optimization and is designed to have two main lobes oriented 90° to each other. This design demonstrates how any farfield pattern can be approximated by setting up a farfield *mask* which works as the goal function for the PSO. However, time constraints prevents this transmitarray to be fabricated and measured.

The farfield mask is defined in UV-space, converted to θ, ϕ-space and applied to each particle. UV-space is the most convenient space to define the mask in since it is easily visualized while still representing the resulting 3D-radiation pattern with high fidelity. The conversion to θ, ϕ space is necessary as all radiating analysis calculations are done in this space. An example of a mask with 10° broadside lobe is shown in Figure 34 in both UV- and angular space.

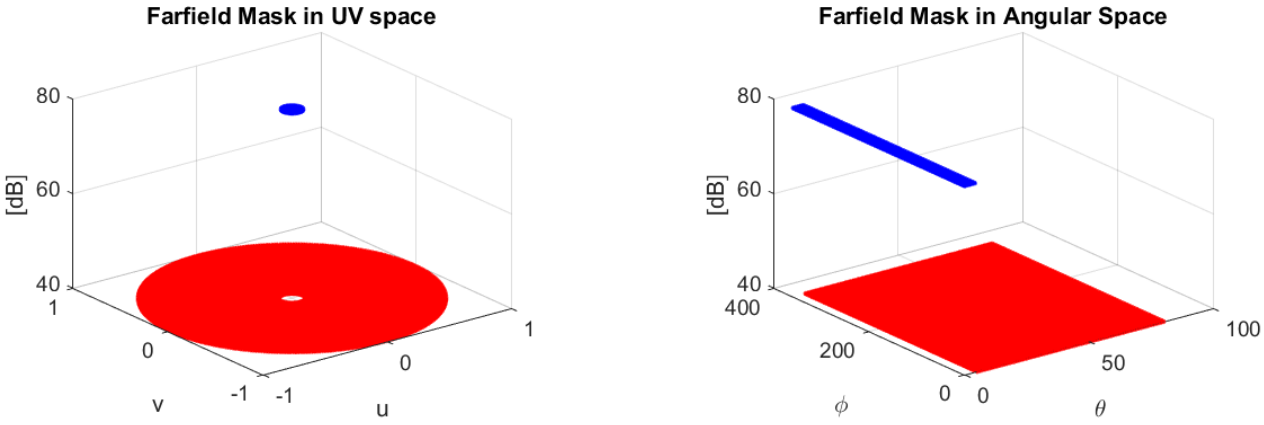

(a) (b)

Figure 34: Example of farfield mask in (a) UV- and (b) θ, ϕ-space. The mask contains a single broadside lobe with 10° beamwidth. The magnitude of the mask is set to correspond to the applicable $20\log_{10}|E|^2$ of the feed. Blue points corresponds to the `lobe` and red points corresponds to the `sidelobe` region.

The goal function take a particle's radiation pattern and the farfield mask as inputs and outputs a scalar error score. The PSO algorithm tries to minimize this score. The mask contains two regions: `lobe` and `sidelobe`, and is used in the calculation of the error score by these rules:

(i) All points below the mask value in the `lobe` region are designated as errors weighted by w_{r0}.

(ii) All points above the mask value in the `lobe` region are not designated as errors.

(iii) All points below the mask value in the `sidelobe` region are not designated as errors.

(iv) All points above the mask value in the `sidelobe` region are designated as errors weighted by w_{r1}.

The resulting cost function is defined as:

$$C = w_{r0} \sum_{\substack{(\theta,\phi)\in \texttt{lobe} \\ \text{and } F(\theta,\phi)<M_{\texttt{lobe}}}} (F(\theta,\phi) - M_{\texttt{lobe}})^2 + w_{r1} \sum_{\substack{(\theta,\phi)\in \texttt{sidelobe} \\ \text{and } F(\theta,\phi)>M_{\texttt{sidelobe}}}} (F(\theta,\phi) - M_{\texttt{sidelobe}})^2 \tag{72}$$

$$F(\theta,\phi) = |E(\theta,\phi)|^2 \tag{73}$$

where $M_{\texttt{lobe}}, M_{\texttt{sidelobe}}$ are the mask values in the `lobe` and `sidelobe` region, respectively, and $F(\theta, \phi)$ is the *value function*, here defined to be the E-field intensity.

For this design, two 10° beamwidth lobes are placed at $\theta = 45°$ and $\phi = 0°$ and $\phi = 90°$. The farfield mask is shown in 35.

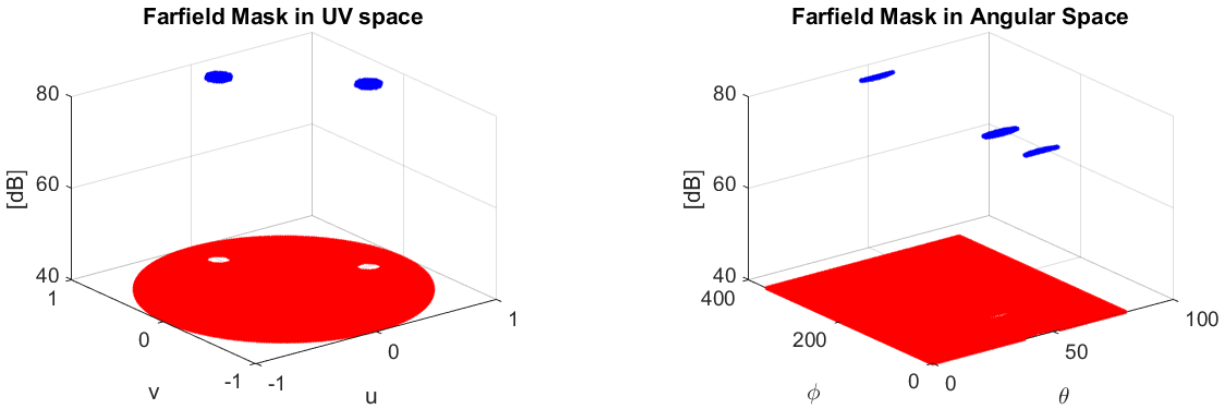

(a) (b)

Figure 35: Farfield mask in (a) UV- and (b) θ, ϕ-space for two lobe, single feed array. The mask contains two main lobes with 10° θ-beamwidth. Blue points corresponds to the `lobe` and red points corresponds to the `sidelobe` region.

The E-patterns after optimization is seen in Figure 36:

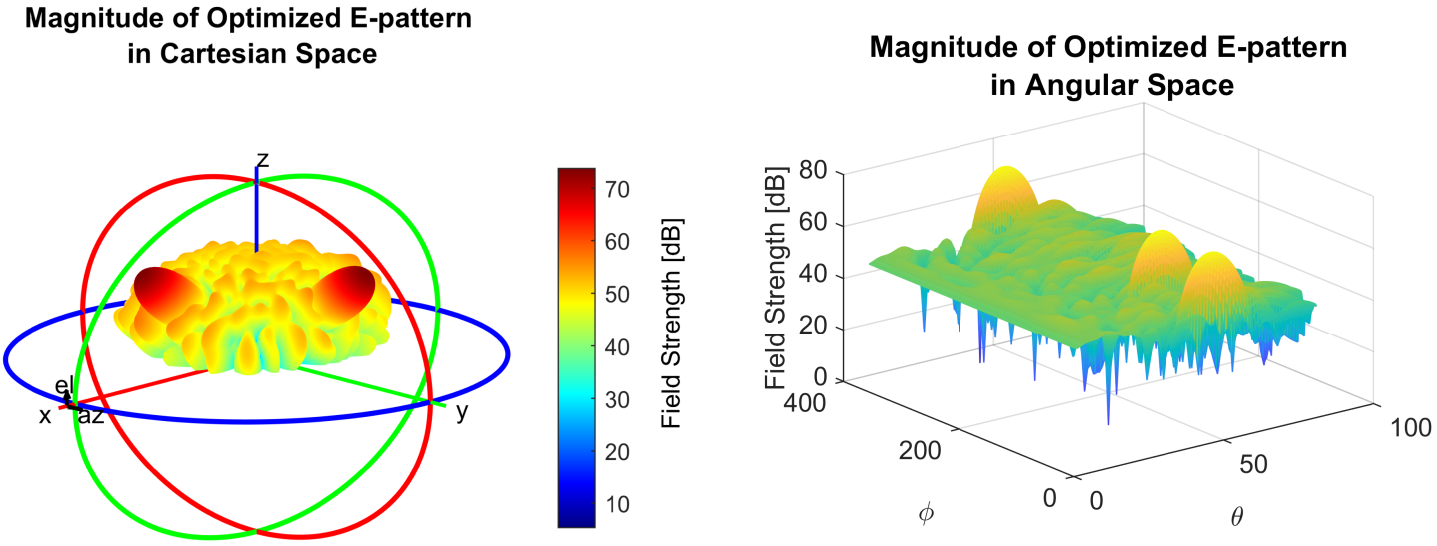

(a) (b)

Figure 36: Result of particle swarm optimization after 500 iterations. (a) shows the radiation pattern in Cartesian space while (b) shows it in angular space.

Finally, the phase and magnitude distribution that results from this PSO is given in 37.

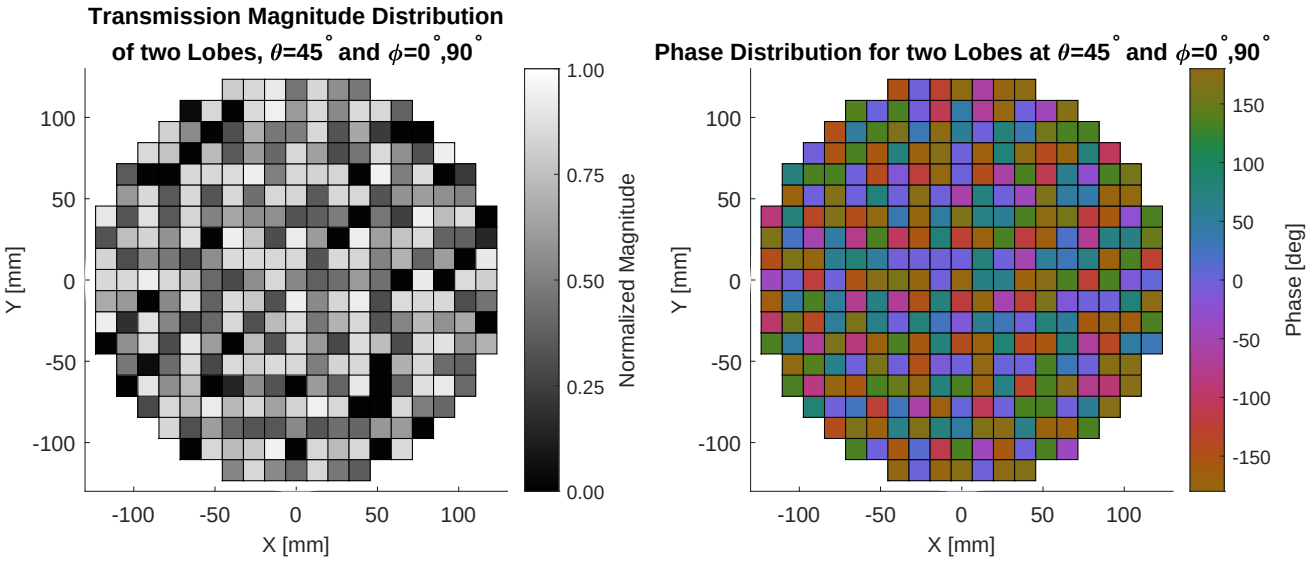

(a) (b)

Figure 37: (a) Magnitude and (b) phase distribution of S_{21} of each unitcell in the transmitarray that generates two main lobes as seen in Figure 35.

3.5 ASSEMBLY

This section describes the mechanical side of the construction of the transmitarray. It consists of two components: structural support and surface suspension. The purpose of the former is to maintain alignment of the unitcells in all three dimensions, while the purpose of the latter is to easily and sufficiently securely index and hold the transmitarray on its mount during measuring.

3.5.1 *Structural Support*

The structural support is made up of spacers and fasteners. Both are made of non conducting materials like Nylon and PLA[10]. The spacers go in between the substrates, maintaining their interlayer distance, and the fasteners clamp the resulting sandwich together. As mention in Section 3.3.1, the substrate is chosen to be 1 mm FR4 glass fiber board. No sample of this substrate was at hand during the design stage, so its rigidity was unknown. A program that quickly designs a support structure for 3D-printing was therefore written.

The structural support program generates a support structure for the array in accordance to two rules: Minimize blockage of the aperture and provide mechanical support. These are reconciled by growing the support from the perimeter into the center while avoiding the centers of each unitcell. By changing the radius at which the support stops to grow, a trade off between stiffness and aperture blockage is achieved, see Figure 38.

10 PLA is a common 3D printing filament material.

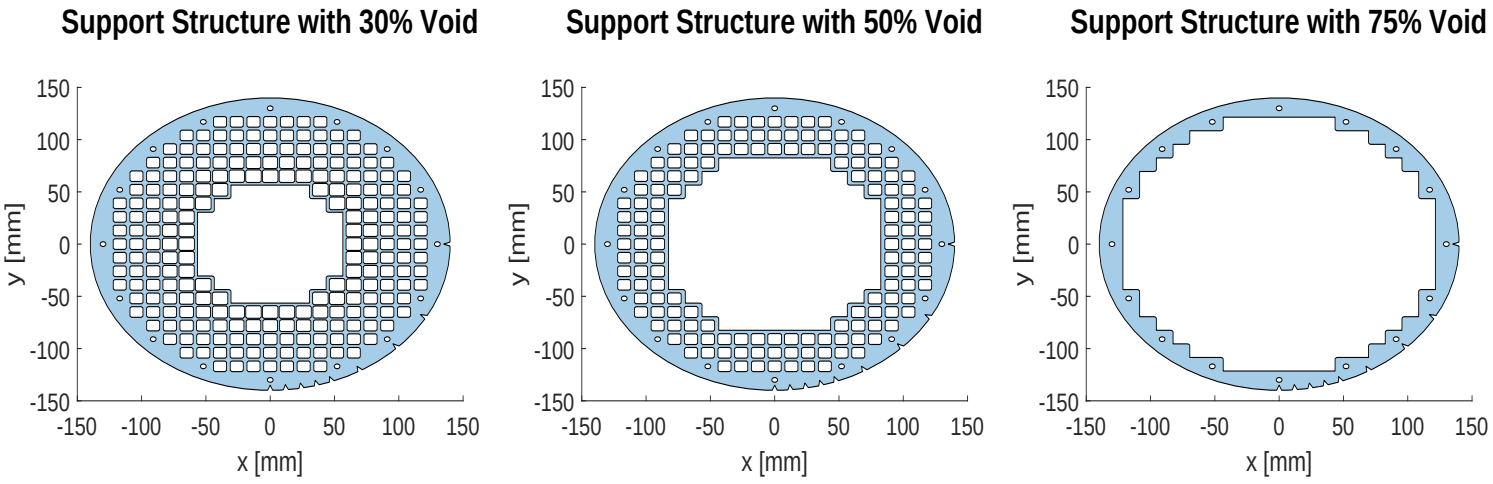

(a) (b) (c)

Figure 38: Result of generating support structures with varying internal void. A larger void results in a smaller blockage of the aperture, but decreases the array stiffness. Both mounting holes and index indents are shown in these figures.

The fasteners are inserting into mounting holes in the array. To minimize coupling effects, these holes are placed as far away from the center as possible and equidistant from adjacent unitcells. The hole locations are found by a program that accepts a list of preferred angles and outputs points that are both nearest to the preferred angle and most distant from neighboring unitcells. The final array uses the angles $[0°, 25°, 45°, 65°] \pm 2°$ in each quadrant.

3.5.2 *Surface Suspension*

The perimeter of the transmitarray is chosen to be circular such that it can easily be rotated in its mount during measuring. In addition, indexing notches are cut out of the edges to facilitate fixture at known rotation angles. These are made triangular to prevent seizing when joined with the mating tooth[11]. The final array has index notches at the angles $[0°, 5°, 10°, 15°, 20°, 30°, 45°, 60°, 90°]$

11 Loose mechanical tolerances are expected as the mounting fixture is made with extrusion 3D-printing.

3.5.3 *The Final Transmitarray*

The shape of the final transmitarray is shown in Figure 39.

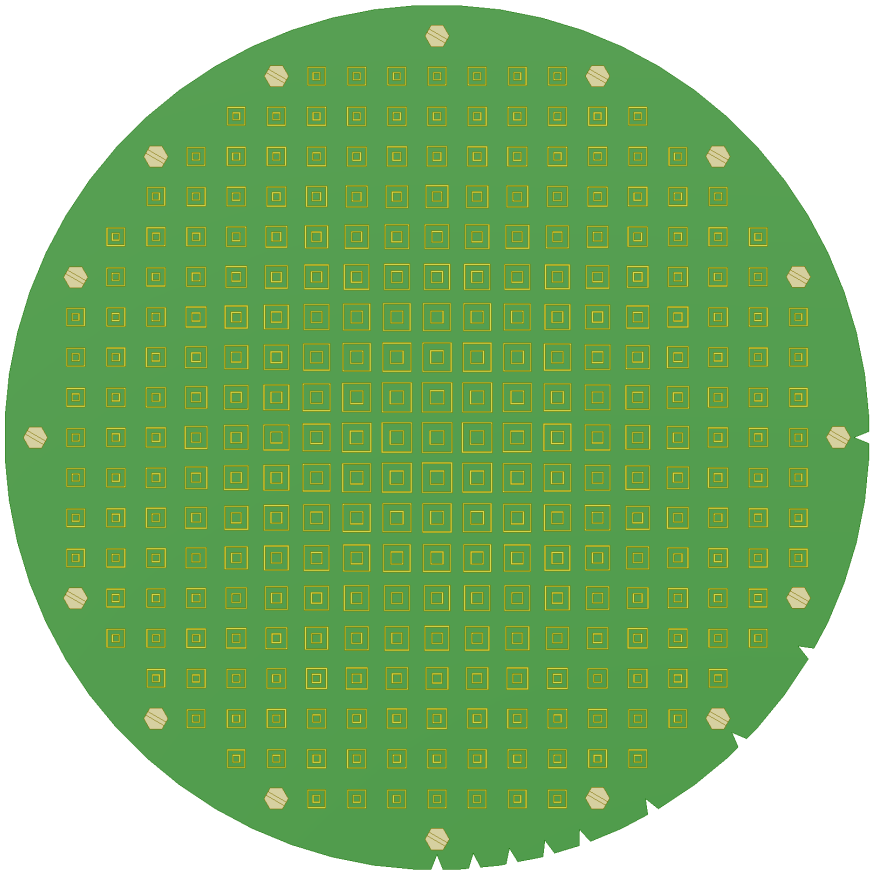

Figure 39: CAD model of the final transmitarray.

4

MEASUREMENT METHOD

The chapter describes the measurement setup for characterizing the transmitarray, followed by detailing the test fixture detailed. The measurement itself is done in an anechoic chamber with a silent zone of 2 m around the measurement platform, certified for 800 MHz and upwards.

4.1 TEST FIXTURE

The purpose of the test fixture is to keep the feed horn aligned with the transmitarray and to set the focus distance. It consists of three parts: the bottom mounting plate, the feed horn mount and the transmitarray mount. An illustration of the complete fixture is given in Figure 40 below.

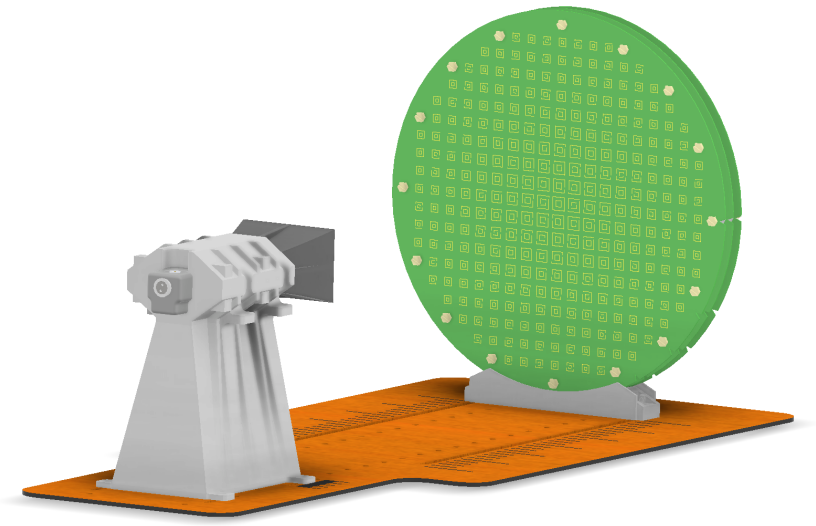

Figure 40: CAD model of the final test fixture used under measurement and characterization of the transmitarray.

The bottom mounting plate holds the feed horn and the transmitarray, and attaches to a rotational platform in the measurement chamber. The former are mounted in slots such that they can be slid along the focus axis, while many possible mounting holes are provides for mounting the plate to the rotation platform. Both are shown in figure Figure 41.

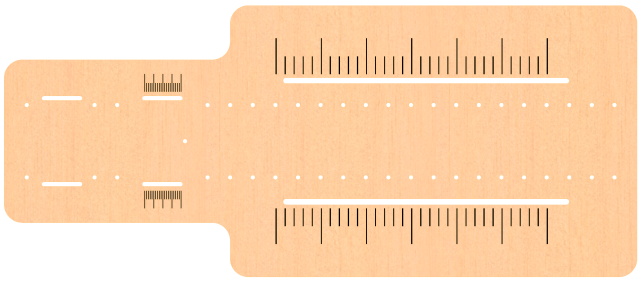

Figure 41: CAD model of the mounting plate that holds the feed horn and transmitarray, and attaches to a rotation platform in the measurement chamber. The feed horn is mounted in the slots on the left and the position of its phase center can be tuned by sliding it along these slots. In a similar manner, the transmitarray is mounted in the slots on the right and the focus distance can be adjusted from 100 mm to 400 mm. All the other holes are possible mounting points for attaching the plate to the rotation platform.

The plate is constructed by two plywood plates with a combined thickness of 9 mm. The slots in the bottom plate is made larger than the upper such that the heads of the nylon bolts can slide freely when the whole fixture lies flat on the rotation platform. This detail is shown in Figure 42.

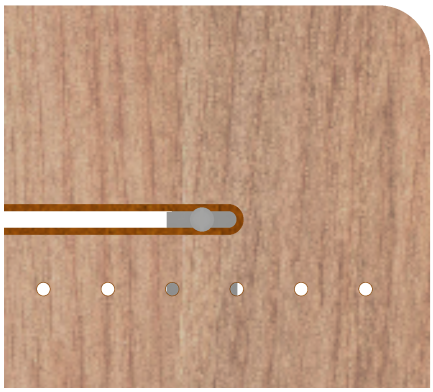

Figure 42: Bottom view of the mounting plate that shows how the head of the bolts for the transmitarray can slide freely.

An exploded view of the feed horn mount is shown in **??**. The clamp around the horn is made such that is follows its shape, leading to a rigid and secure hold.

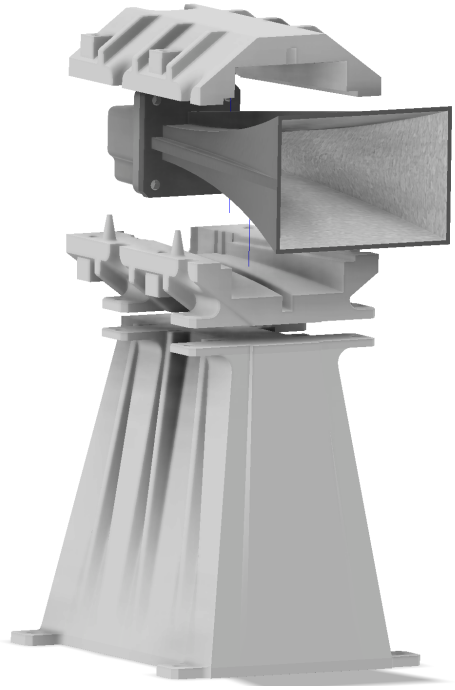

Figure 43: Exploded view of the feed horn mount. The mount parts are made from 3D printed PLA.

The mount for the transmitarray is shown in Figure 44. It is a simple curve section with an indexing notch that fits into the indexing notches in the array.

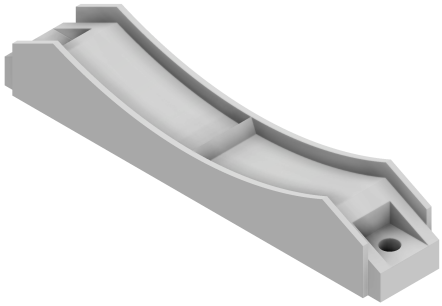

Figure 44: CAD model of the transmitarray mounting. The transmitarray is not firmly secured into the mount, but is held in place by friction from the two raised edges. This facilitates easy change of rotation of the transmitarray during measurement.

5

RESULTS - SIMULATION AND MEASUREMENT

This section will present the central results from simulation and measurement of the implemented transmitarray antenna, but not from the single-fed multi-lobe transmitarray simulations in Section 3.4.2. Time did unfortunately permit a through discussion of the latter.

The first result that is presented is the normalized power pattern of the simulated and measured feed antenna, see Figure 45. The half power beam width of the simulated and measured antenna is respectively 23.9° and 22.8°. It is apparent that the two curves correspond to a high degree, and it verifies that the feed pattern used in the transmitarray simulations is accurate.

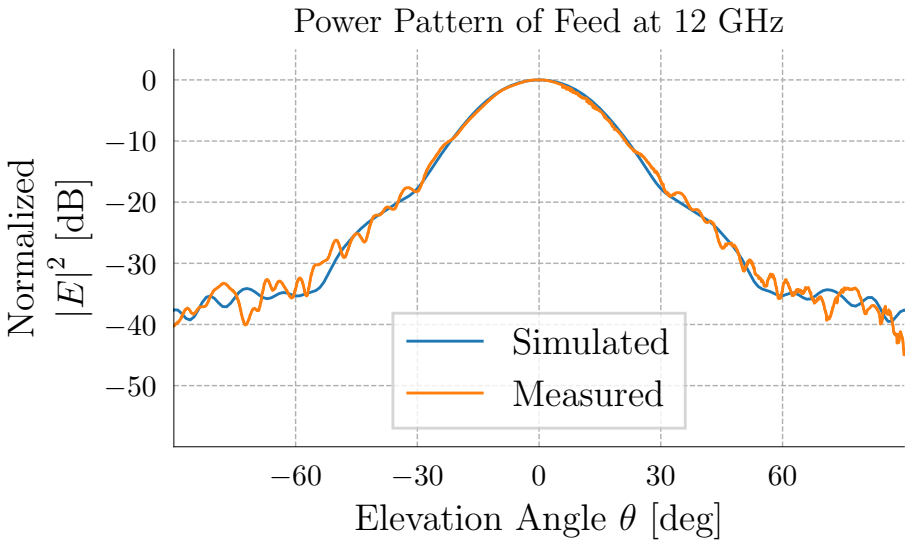

Figure 45: Normalized power pattern for simulated and measured feed horn at 12 GHz. The physical horn is measured while rotating it around its phase center. This phase center was found by adjusting the position of the horn such that the variation in phase over a 180° rotation was lowest. The resulting position of the phase center coincided with the predicted location within a few millimeters.

5.1 GAIN AT DESIGNED FOCUS DISTANCE

Two figures for the design focus distance of $F = 400\,\text{mm}$ are presented below. The first, 46, shows the normalized power pattern of both the simulated and measured transmitarray. It noted that half power beam width matches within 1.5 degrees, 6.1° for simulated vs 4.7° for measured, but the levels of the side lobes does not.

The second plot, Figure 47, shows the simulated and measured power patterns of both the feed and the transmitarray. The simulated and measured curved has been normalized with respect to their feeds, such that the power scaling is the same. Clearly, the gain of the measured transmitarray is many dB lower than the simulated one, with 9.4 dB vs 3.4 dB.

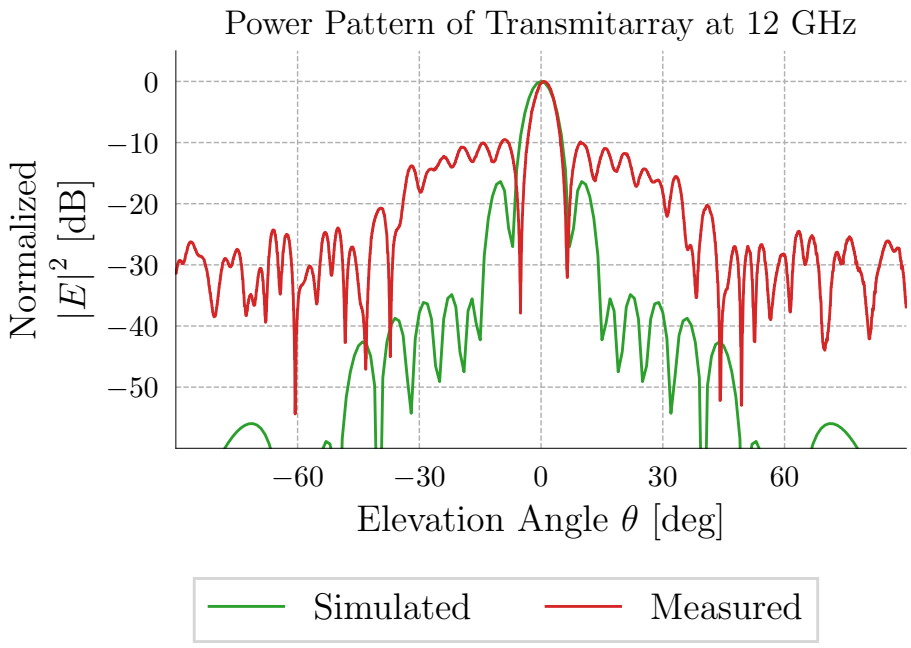

Figure 46: Normalized power pattern of simulated and measured transmitarray at the designed focus distance of $F = 400\,\text{mm}$.

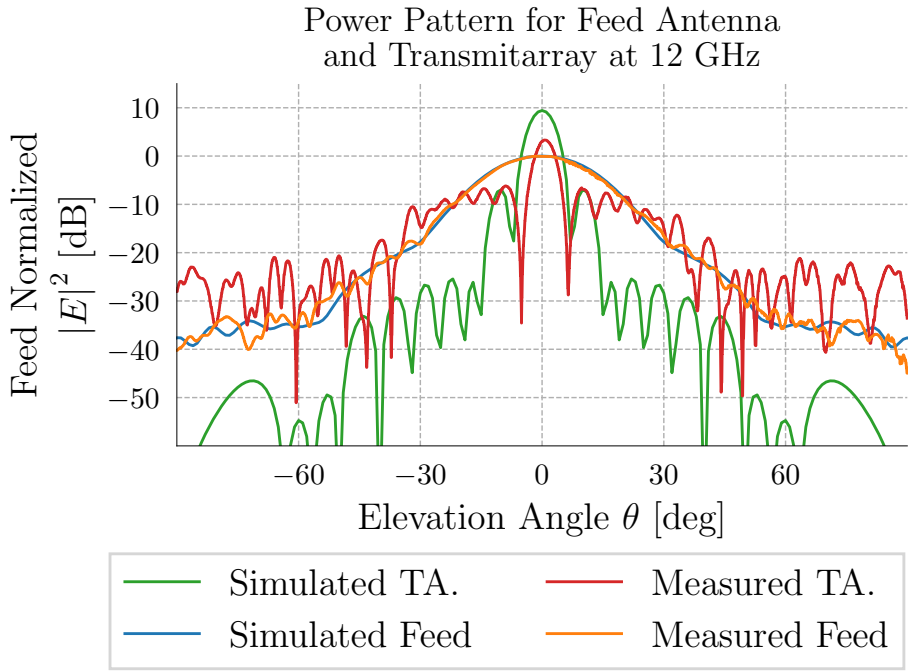

Figure 47: Simulated and measured power plot of both the feed antenna and the transmitarray at a focus distance of $F = 400\,\text{mm}$. TA. = transmitarray. In order to compare the simulation results with the measured ones, the feed antenna curves are used as reference levels. First, the simulated feed antenna curve is normalized, followed by level adjusting the measured data such that the measured and simulated feed antenna curve coincide at their maxima.

5.1.1 *Gain at other Frequencies*

Next, the gain and HPBW for frequencies in the vicinity of 12 GHz is investigated, see Figure 48. Two things are apparent from this plot: Both the gain and the HPBW is higher for the simulated transmitarray than the measured one; and there is a pronounced ripple in the HPBW for the measured array.

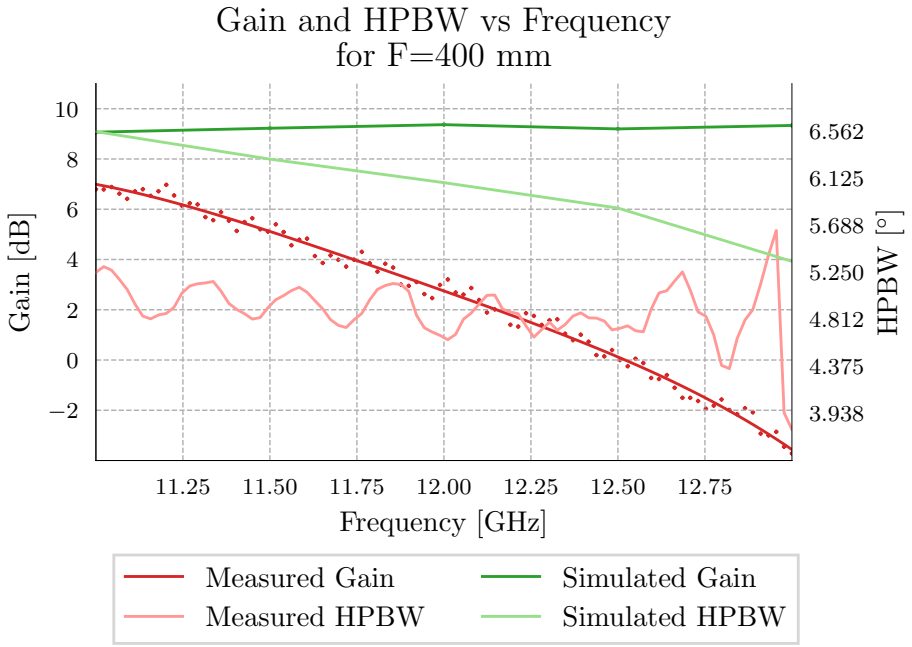

Figure 48: Simulated and measured gain and HPBW of the transmitarray at a focus distance of $F = 400$ mm. The simulated curves are in green and the measured curves are in red. Lighter colors correspond to HPBW. For each frequency point on the simulated curves, the farfield and directivity for the feed horn correspond to this frequency. The same goes for the radiation analysis calculation. This is not however the case for the unit cells, i.e. the S_{21} parameters used in this simulation are all the same as that for 12 GHz. For the measured gain data, the calculated gain points are shown as individual points while a regression fit is shown as a solid curve.

5.2 DIRECTIVITY AND GAIN AT OTHER FOCUS DISTANCES

Below follows a series of plots where the focus distance varied within $F \in [200, 250, 300, 350, 420]$, but otherwise identical to Figure 48 above. These corresponds to the physical extremes of the test jig that holds the transmitarray. The points for the measured values of gain is interpolated with an high order polynomial such that the trend stands out.

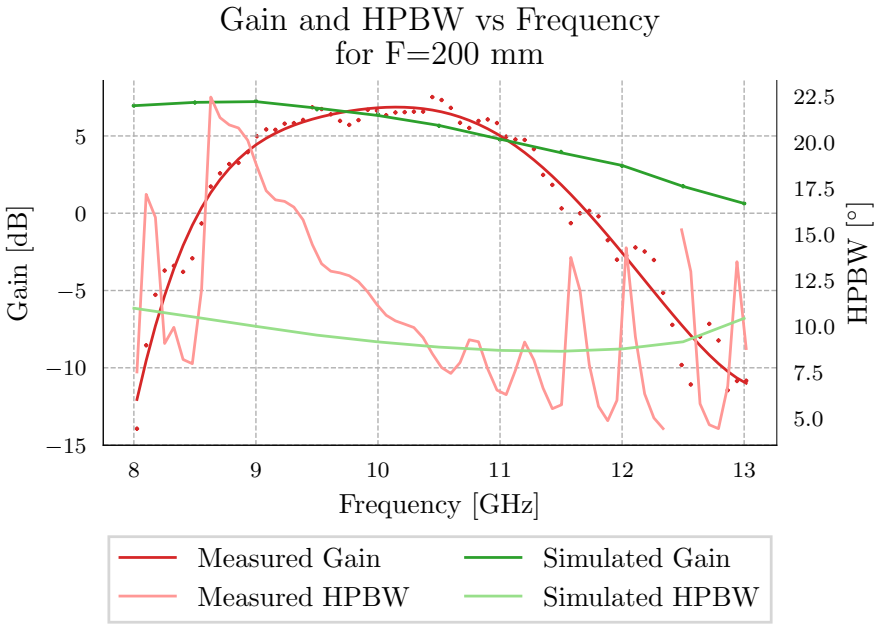

Figure 49: Simulated and measured gain and HPBW of the transmitarray at a focus distance of $F = 200\,\text{mm}$. The simulated curves are in green and the measured curves are in red. Lighter colors correspond to HPBW. For the measured gain data, the calculated gain points are shown as individual points while a regression fit is shown as a solid curve.

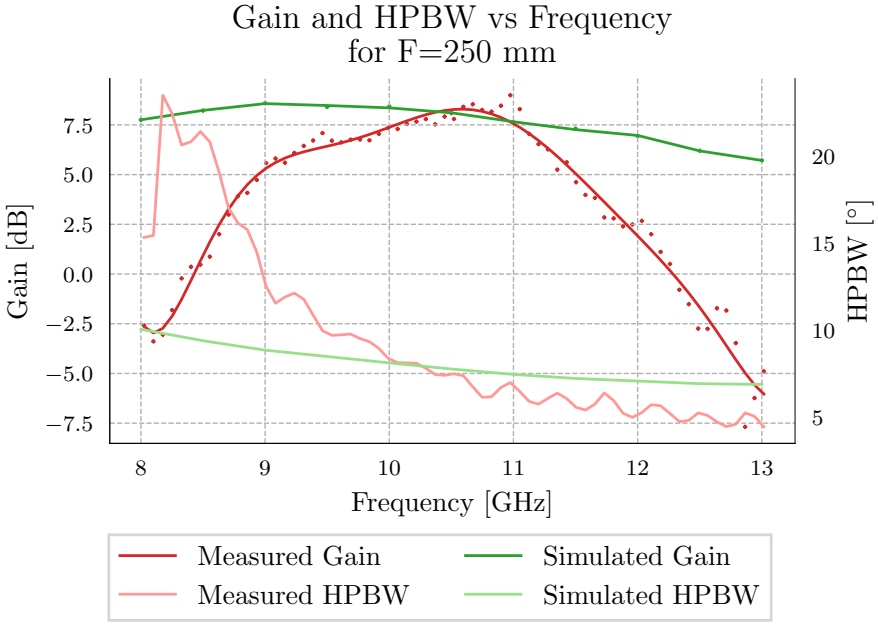

Figure 50: Simulated and measured gain and HPBW of the transmitarray at a focus distance of $F = 250\,\text{mm}$. The simulated curves are in green and the measured curves are in red. Lighter colors correspond to HPBW. For the measured gain data, the calculated gain points are shown as individual points while a regression fit is shown as a solid curve.

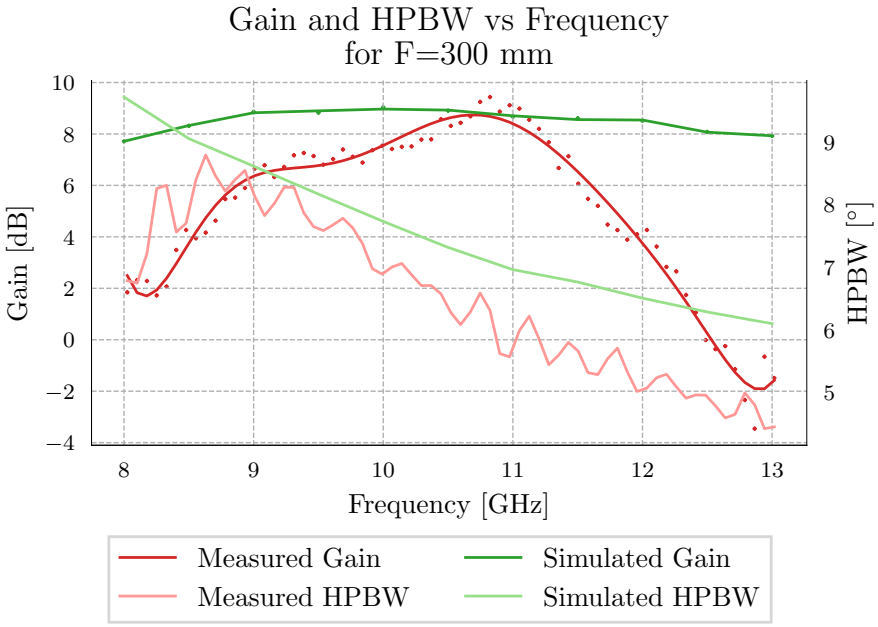

Figure 51: Simulated and measured gain and HPBW of the transmitarray at a focus distance of $F = 300$ mm. The simulated curves are in green and the measured curves are in red. Lighter colors correspond to HPBW. For the measured gain data, the calculated gain points are shown as individual points while a regression fit is shown as a solid curve.

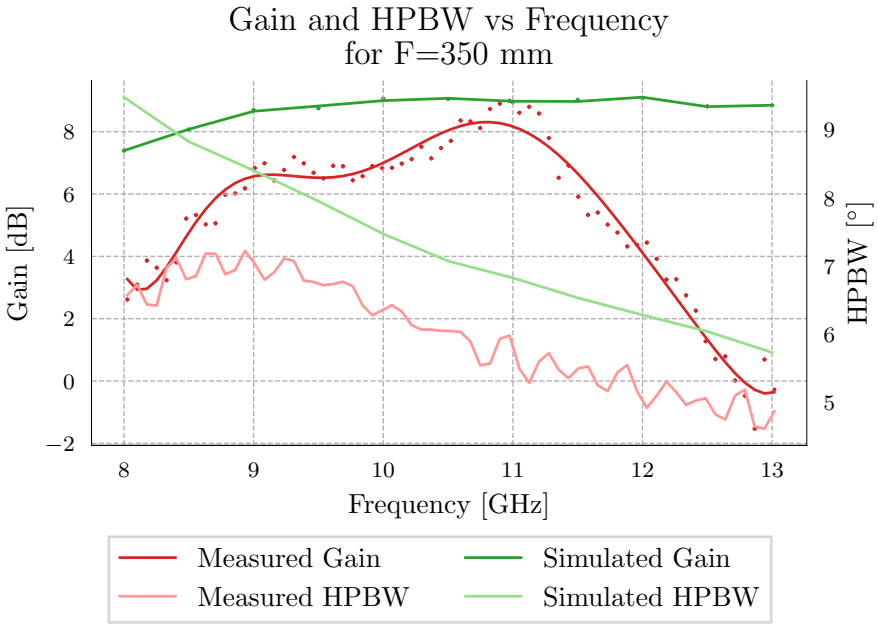

Figure 52: Simulated and measured gain and HPBW of the transmitarray at a focus distance of $F = 350$ mm. The simulated curves are in green and the measured curves are in red. Lighter colors correspond to HPBW. For the measured gain data, the calculated gain points are shown as individual points while a regression fit is shown as a solid curve.

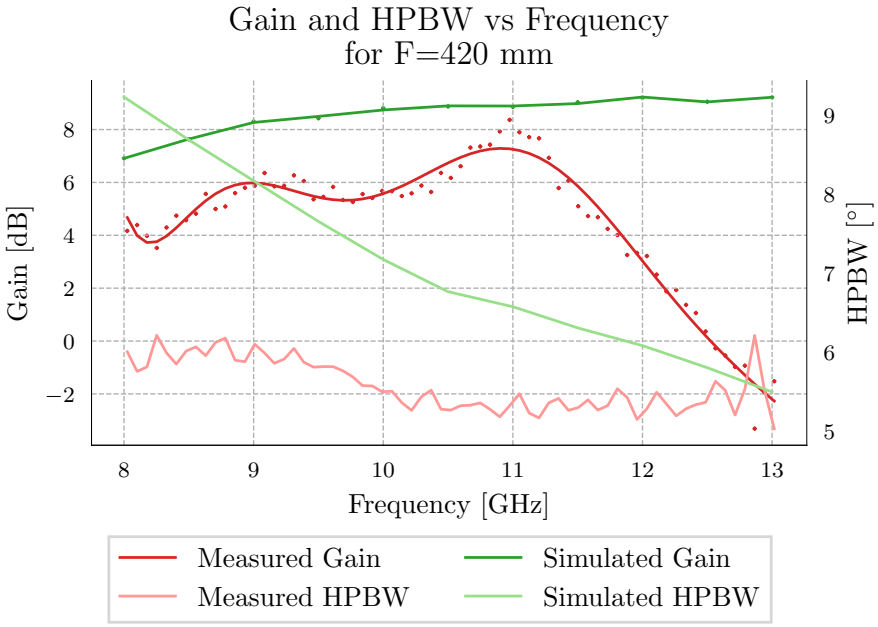

Figure 53: Simulated and measured gain and HPBW of the transmitarray at a focus distance of $F = 420$ mm. The simulated curves are in green and the measured curves are in red. Lighter colors correspond to HPBW. For the measured gain data, the calculated gain points are shown as individual points while a regression fit is shown as a solid curve.

Lastly, Table 2 lists the values for gain at 12 GHz and the location for maximum measured gain. It is apparent that the latter holds steady at 10.9 GHz and hovers around 9 dB.

Table 2: Simulated and measured gain at 12 GHz for varying focus distances. Measured maximum gain is also listed. The designed parameters is 12 GHz at a focus distance of $F = 400$ mm. The values for maximum measured gain for $F = 400$ mm is empty since lower frequencies than 11 GHz was not measured at this focus distance.

Focus Distance	**Gain at 12 GHz [dB]**		**Maximum measured gain**	
	Simulated	**Measured**	**Gain [dB]**	**Frequency [GHz]**
200 mm	3.06	-2.73	7.5	10.45
250 mm	6.94	2.67	8.99	10.97
300 mm	8.51	4.27	9.43	10.82
350 mm	9.08	4.44	8.99	10.97
400 mm	9.43	3.44	-	-
420 mm	9.20	3.22	8.37	10.97

6

DISCUSSION

It is apparent from the results in Chapter 5 that the realized transmitarray performed considerably worse than the designed transmitarray. At the designed focus distance of $F = 400$ mm and center frequency of 12 GHz, the difference in gain between the simulated and measured transmitarray is 9.4 dB – 3.4 dB = 6 dB. Furthermore, the sidelobes of the realized transmitarray is substantially higher than the simulated one by > 5 dB at the lowest and > 20 dB at the highest. In contrast, the half power beam width for the measured transmitarray is narrower than the simulated one by 1.4°.

There are three principal causes that could account for the discrepancy between the simulated and measured results. Firstly, the field pattern of the feed used in the design and simulation could be wrong. This is however most likely not the case since the field pattern of the simulated feed horn corresponds well with the measured one.

Secondly, the implementation of radiation analysis based on (12) used to calculate the field pattern and gain could contain an error. This is probable given the many steps involved in the processes going from raw unit cell simulation data to fabrication files.

It is however believed that any such errors only accounts for a fraction of the discrepancy in gain. The primary reason for this belief is that the calculation implementations was tested and compared to implementations from a third party[1]. In addition, the loss in gain from phase range truncation was shown by Figure 31 to be ≈ 1.5 dB for 64 elements, giving an indication that small implementation errors likely will be in the range of 1 dB[2].

The final principal cause that could account for the difference between simulated and excepted results is differences in the simulated and actual FR4 substrate. FR4 is not a high performance substrate at RF-frequencies, and the used parameters of $\varepsilon_r = 4$ and $\tan\delta = 0.012$ at 12 GHz is likely not accurate values.

1 Matlab's extensive libraries for EM-simulation and array antenna analysis was used as comparison. These libraries could not be used directly in the project because of incompatibilities and long execution times.

2 The basis for this reasoning is that any implementation errors most likely lies in the portion of the code that could not be compared to a third party's results. This portion is dominantly the mapping between unit cell S_{21} simulation data to the desired phase distribution of the surface.

The gain curves in figures 48 to 53 all shows a peak at 11 GHz followed by a sharp decline for higher frequencies. This indicates that the center frequency is lower and substrate permittivity is higher than $\varepsilon_r = 4$, based on the relation $f \propto \frac{c}{2\pi\sqrt{\varepsilon_r \mu_r}}$. Furthermore, the sharp decline suggest that the loss increases quickly above 11 GHz and that $\tan\delta$ is significantly higher than 0.012.

The focus distance for the measured transmitarray is shorter than the simulated one. As can be seen from Table 2, the peak gain of the simulated array is achieved at $F = 400$ mm at 12 GHz, while it is $F = 300$ mm for the measured one at 11 GHz. This can also be attributed to lower center frequency, strengthening the case that $\varepsilon_r > 4$.

7

CONCLUSION

A design of a 12 GHz collimating transmitarray is presented in this thesis, together with a demonstration of using particle swarm optimization to synthesize the phase distribution for a single fed dual lobe transmitarray. Both are based on three layered square double loop unit cells where the diameter of the loops determine the phase shift. The collimating transmitarray is fabricated on a FR-4 substrate and measured in anechoic chamber.

Simulations of the collimating transmitarray displays a peak gain of 9.43 dB at the designed focus distance of $F = 400$ mm and 12 GHz, while measurements shows a meager 3.44 dB gain at the same frequency and focus distance. Further investigations shows that the center frequency of the fabricated array lies in the vicinity of 11 GHz and achieves a peak gain of 9.43 dB at a focus distance of $F = 300$ mm. This discrepancy is probably due to higher permittivity in the substrate than was used in the simulation.

The results from the particle swarm optimization shows great promise for creating transmitarrays that achieves an arbitrary desired far field. Synthesizing a phase distribution for two separate lobes at ($\theta = 45°$, $\phi = 0°$) and ($\theta = 45°$, $\phi = 45°$) shows clear attainment of the goal far field mask after 500 iterations. This demonstrates the flexibility of transmitarray technology to modify the wavefront of a given feed antenna through numerical optimization techniques.

The choice of using ordinary FR4 substrate rather than an RF substrate with clearly defined permittivity and low loss did cause errors between the excepted and actual transmitarray. But it still works well enough to demonstrate the principle of using a transmitarray as an electromagnetic lens to collimate the field from a horn antenna, albeit at a lower frequency.

8

FUTURE WORK

There are numerous aspects of transmitarrays that deserves further study. One may categorize these as: feed, element size, element type and active arrays.

Many works on transmitarrays approximates the feed as a raised cosine. Work during this thesis did however show that using simulated field pattern from the intended feed antenna changes the necessary phase distribution. This is also excepted to be a significant factor when designing with other feeds than a horn, like a single dipole or path.

Another common approximation is that the transmitarray exists in the far field. This is convenient, but practical applications would benefit from lenses that can be placed as close to the feed antenna as possible. Examining transmitarrays located in the near-field is thus interesting. Electromagnetic lenses in the near field has already been done with metamaterials, but the author is unaware if there exists planar transmitarrays that does the same.

The boundary between a proper metamaterial lens and a lens based on EBG structures does not appear to have been investigated in existing literature. There exists many studies for metamaterials and EBG on their own, but what happens with the performance of of lenses when the element sizes lies between the clear cut boundaries of $\lambda/10$ and $\lambda/2$?

Element types with higher performance and modifies the polarization is also a natural progression from the work done in this thesis. Rotation of the element with respect to other elements changes polarization and may impose different phase distributions for different polarizations. The S_{21} limits described here only holds for high angle of incidence. Elements that maintain their characteristics for shallow angles is another interesting aspect to study.

Lastly, the use of active elements that can change their S_{21} characteristics and allow for electronically controlled arrays is especially interesting. FPGA devices can drive varactors or RF-switches and quickly change the farfield, essentially becoming a phased array but with only one feed antenna.

A

DERIVATION OF TRANSMISSION COEFFICIENT FOR IDEAL UNITCELLS

This derivation is based on [2], where four assumptions are used to get an expression for the transmission coefficient S_{21}:

1. The S-matrix is reciprocal, meaning that the transmission of a signal does not depend on the direction of propagation.

$$\mathbf{S}^T = \mathbf{S} \tag{74}$$

which gives

$$S_{21} = S_{12} \tag{75}$$

2. The S-matrix is symmetrical, meaning that the network is identical looking into each port.

$$S_{11} = S_{22} \tag{76}$$

3. The S-matrix is lossless.

$$\sum_{m}^{M} |S_{mn}|^2 = 1 \quad \text{for all } n \tag{77}$$

which gives

$$|S_{11}|^2 + |S_{21}|^2 = 1 \tag{78}$$
$$|S_{12}|^2 + |S_{22}|^2 = 1 \tag{79}$$

4. Higher order harmonics is small and can be neglected. By Fresnel's law:

$$S_{21} - S_{11} = 1 \tag{80}$$

To get the desired expression, we begin by combining (78) with (79) and use the identity $|z| = \sqrt{z \cdot z^*}$[24]:

$$\begin{aligned} |S_{12}|^2 + |S_{22}|^2 &= |S_{11}|^2 + |S_{21}|^2 \\ S_{11}S_{12}^* + S_{21}S_{22}^* &= 0 \end{aligned} \tag{81}$$

Substituting (75) into (81):

$$\begin{aligned} S_{11}S_{21}^* + S_{21}S_{11}^* &= 0 \\ |S_{11}|e^{j\angle S_{11}}|S_{21}|e^{-j\angle S_{21}} + |S_{21}|e^{j\angle S_{21}}|S_{11}|e^{-j\angle S_{11}} &= 0 \\ e^{j\angle S_{11}}e^{-j\angle S_{21}} + e^{j\angle S_{21}}e^{-j\angle S_{11}} &= 0 \\ e^{j\angle S_{11}}e^{-j\angle S_{21}} &= -e^{j\angle S_{21}}e^{-j\angle S_{11}} \\ e^{2j\angle S_{11}} &= -e^{2j\angle S_{21}} \end{aligned} \tag{82}$$

we take the argument of (82) and get

$$\angle S_{11} = \angle S_{21} \pm \frac{\pi}{2} \tag{83}$$

This result is used in (80):

$$\begin{aligned} |S_{21}|e^{j\angle S_{21}} - |S_{11}|e^{j\angle S_{11}} &= 1 \\ |S_{21}|e^{j\angle S_{21}} - |S_{11}|e^{j\angle S_{21}\pm\frac{\pi}{2}} &= 1 \\ |S_{21}| - |S_{11}|e^{\pm j\frac{\pi}{2}} &= e^{-j\angle S_{21}} \\ |S_{21}| \pm j|S_{11}| &= e^{-j\angle S_{21}} \\ |S_{21}| \pm j|S_{11}| &= \cos(\angle S_{21}) - j\sin(\angle S_{21}) \end{aligned} \tag{84}$$

The last expression (84) is decomposed into real and imaginary parts to get the final relation:

$$|S_{21}| = \cos(\angle S_{21}) \tag{85}$$

$$|S_{11}| = \pm\sin(\angle S_{21}) \tag{86}$$

B

SIMULATION RESULTS FOR ONE LAYER UNIT CELLS WITH ONLY METAL LAYER

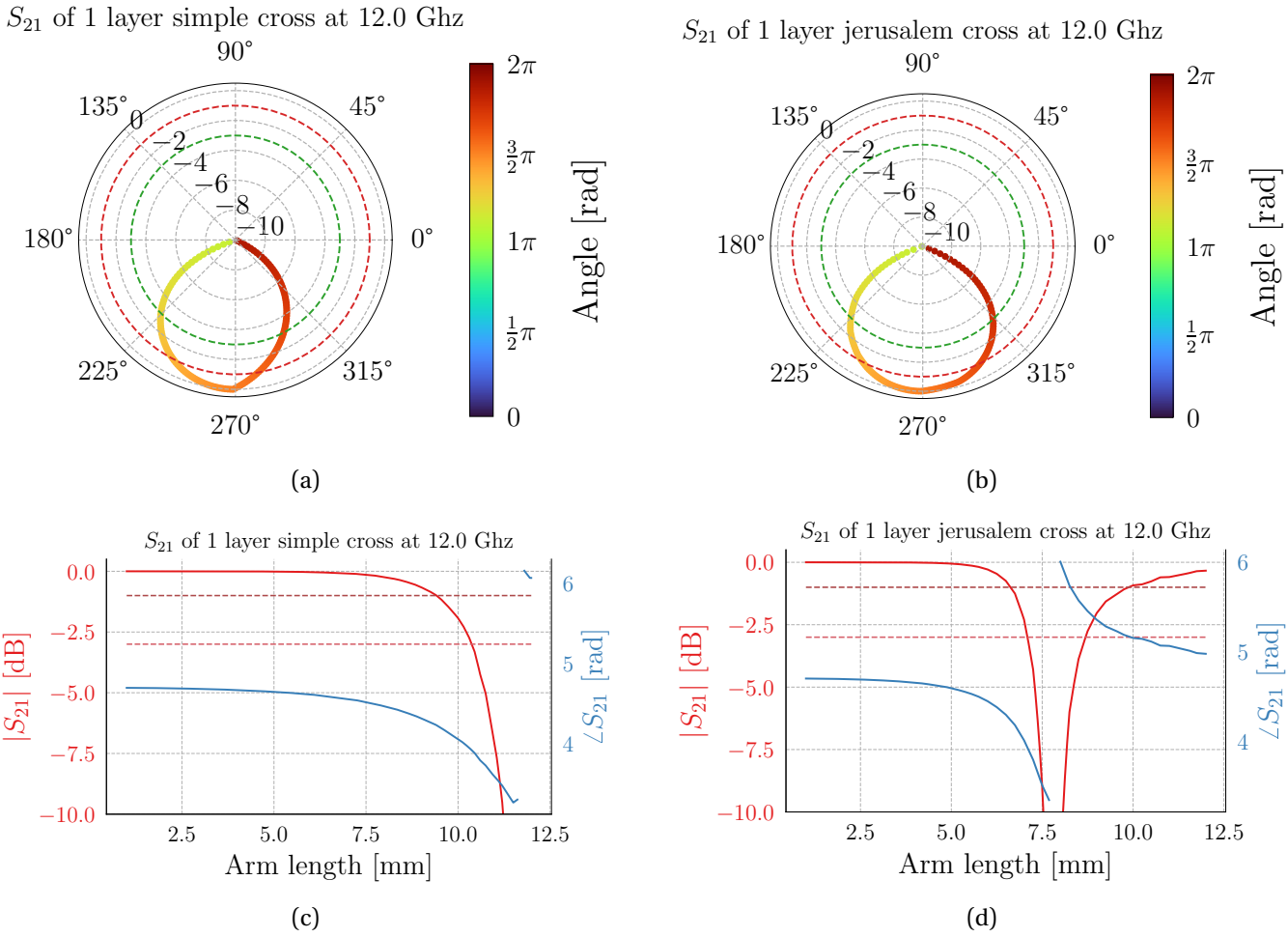

Figure 54: Full wave simulation results of the transmission coefficient S_{21} for simple cross and Jerusalem cross unit cells. The structure of the cells are seen in Figure 24, but only the metal layer is used in these simulations. The the magnitude is given in dB for the polar and line plots. The dotted lines in all the graphs are the –1 dB and –3 dB magnitude lines. All unit cells have the same periodicity of $a_x = a_y = \lambda/2 = 12.49$ GHz and have Floquet ports on each lateral side of the unit cell. All simulations were done with inclination angle of $\theta = 90°$.

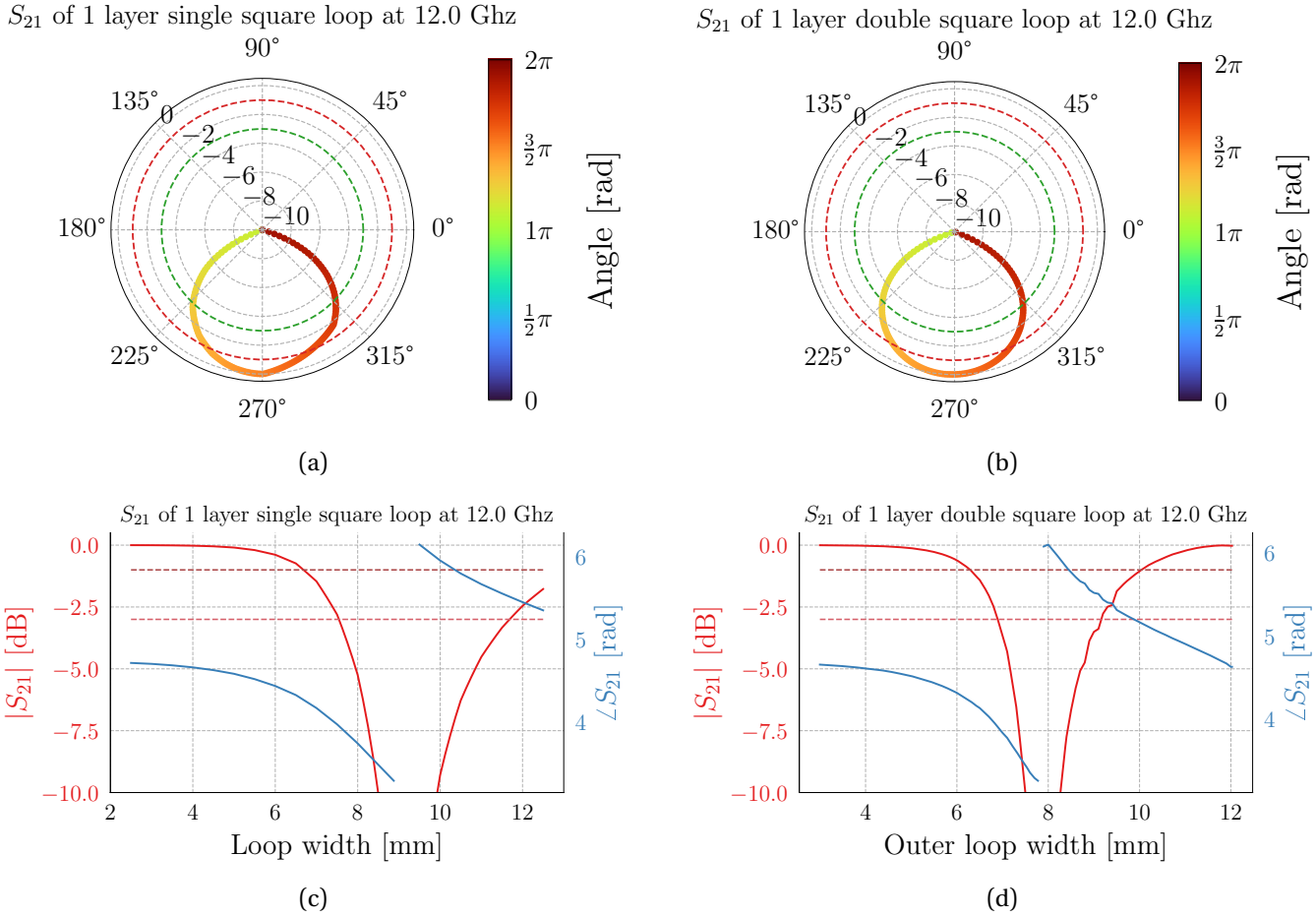

Figure 55: Full wave simulation results of the transmission coefficient S_{21} for single square loop and double square loop unit cells. For the double square loop unit cell, the separation between the inner and outer loops is $0.22 \cdot$ width of the outer loop. The structure of the cells are seen in Figure 24, but only the metal layer is used in these simulations. The the magnitude is given in dB for the polar and line plots. The dotted lines in all the graphs are the –1 dB and –3 dB magnitude lines. All unit cells have the same periodicity of $a_x = a_y = \lambda/2 = 12.49$ GHz and have Floquet ports on each lateral side of the unit cell. All simulations were done with inclination angle of $\theta = 90°$.

BIBLIOGRAPHY

[1] Abbas Abbaspour-Tamijani, K. Sarabandi, and G.M. Rebeiz. "A millimetre-wave bandpass filter-lens array." In: *Microwaves, Antennas & Propagation, IET* 1 (May 2007), pp. 388–395. DOI: 10.1049/iet-map:20050295.

[2] Ahmed H. Abdelrahman, Atef Z. Elsherbeni, and Fan Yang. "Transmission Phase Limit of Multilayer Frequency-Selective Surfaces for Transmitarray Designs." In: *IEEE Transactions on Antennas and Propagation* 62.2 (2014), pp. 690–697. DOI: 10.1109/TAP.2013.2289313.

[3] Ahmed H. Abdelrahman, Fan Yang, Atef Z. Elsherbeni, and Payam Nayeri. *Analysis and design of transmitarray antennas*. Morgan & Claypool Publishers, 2017.

[4] Constantine A. Balanis. *Antenna theory: analysis and design*. 4th ed. Wiley Blackwell, 2016.

[5] Christophe Caloz and Tatsuo Itoh. *Electromagnetic Metamaterials: Transmission Line Theory and Microwave Applications: The Engineering Approach*. John Wiley & Sons, Inc, 2005, pp. 1–352. ISBN: 0471669857. DOI: 10.1002/0471754323.

[6] David K. Cheng. *Field And Wave Electromagnetics*. 2nd ed. Edinburgh Gate: Pearson, 2014. ISBN: 1-292-02656-1.

[7] Tie Jun Cui, David R. Smith, and Ruopeng Liu. *Metamaterials: Theory, Design, and Applications*. 2010, pp. 1–367. ISBN: 9781441905727. DOI: 10.1007/978-1-4419-0573-4.

[8] Tie Jun Cui, Wen Xuan Tang, Xin Mi Yang, Zhong Lei Mei, and Wei Xiang Jiang. *Metamaterials Beyond Crystals, Noncrystals, and Quasicrystals*. Chapman and Hall/CRC, 2016.

[9] Bhavani Devireddy, Ang Yu, Fan Yang, and Atef Z Elsherbeni. "Gain and bandwidth limitations of reflectarrays." In: *ACES Journal-Applied Computational Electromagnetics Society* 26.2 (2011), p. 170.

[10] Nicolas Gagnon, Aldo Petosa, and Derek A. McNamara. "Comparison between conventional lenses and an electrically thin lens made using a phase shifting surface (PSS) at Ka Band." In: *2009 Loughborough Antennas Propagation Conference*. 2009, pp. 117–120. DOI: 10.1109/LAPC.2009.5352545.

[11] Nicolas Gagnon, Aldo Petosa, and Derek A. McNamara. "Thin Microwave Quasi-Transparent Phase-Shifting Surface (PSS)." In: *IEEE Transactions on Antennas and Propagation* 58.4 (2010), pp. 1193–1201. DOI: 10.1109/TAP.2010.2041150.

[12] John Huang and Encinar José A. *Reflectarray antennas*. IEEE Press, 2008.

[13] Shinji Kamada, Naobumi Michishita, and Yoshihide Yamada. "Metamaterial lens antenna using dielectric resonators for wide angle beam scanning." In: *2010 IEEE Antennas and Propagation Society International Symposium*. 2010, pp. 1–4. DOI: 10.1109/APS.2010.5561780.

[14] Min Liang, Wei-Ren Ng, Kihun Chang, Kokou Gbele, Michael E. Gehm, and Hao Xin. "A 3-D Luneburg Lens Antenna Fabricated by Polymer Jetting Rapid Prototyping." In: *IEEE Transactions on Antennas and Propagation* 62.4 (2014), pp. 1799–1807. DOI: 10.1109/TAP.2013.2297165.

[15] Martin Lima. "Overview Of Electromagnetic Metamaterials And Electromagnetic Band Gap Structures For Use In Antenna Engineering." IES. Semester Project. NTNU, Dec. 2020.

[16] J.T. Loane and D.R. Tanner. "General constrained lens or reflector equations with relation to the Abbe sine condition." In: *IEEE Antennas and Propagation Society International Symposium. 1996 Digest*. Vol. 2. 1996, 926–927 vol.2. DOI: 10.1109/APS.1996.549747.

[17] Carolina Mateo-Segura, Amy Dyke, Hazel Dyke, Sajad Haq, and Yang Hao. "Flat Luneburg Lens via Transformation Optics for Directive Antenna Applications." In: *IEEE Transactions on Antennas and Propagation* 62.4 (2014), pp. 1945–1953. DOI: 10.1109/TAP.2014.2302004.

[18] D. McGrath. "Planar three-dimensional constrained lenses." In: *IEEE Transactions on Antennas and Propagation* 34.1 (1986), pp. 46–50. DOI: 10.1109/TAP.1986.1143726.

[19] Thomas A. Milligan. *Modern Antenna Design*. 2nd ed. John Wiley & Sons, 2005.

[20] Ben Munk. *Frequency selective surfaces: theory and design*. 1st ed. John Wiley, 2000.

[21] P. Nayeri. "Advanced design methodologies and novel applications of reflectarray antennas." In: 2012.

[22] Payam Nayeri, Fan Yang, and Atef Z. Elsherbeni. *Reflectarray antennas theory, designs and applications*. Wiley, 2018.

[23] *Negative-refraction metamaterials : fundamental principles and applications*. eng. Hoboken, N.J: IEEE Press, 2005. ISBN: 0471601462.

[24] David M. Pozar. *Microwave engineering*. 4th ed. John Wiley, 2012.

[25] Singiresu S. Rao. *Engineering optimization: theory and practice*. 4th ed. John Wiley & Sons, 2009.

[26] J. Ruze. "Wide-Angle Metal-Plate Optics." In: *Proceedings of the IRE* 38.1 (1950), pp. 53–59. DOI: 10.1109/JRPROC.1950.232789.

[27] B. Schoenlinner, Xidong Wu, J.P. Ebling, G.V. Eleftheriades, and G.M. Rebeiz. "Wide-scan spherical-lens antennas for automotive radars." In: *IEEE Transactions on Microwave Theory and Techniques* 50.9 (2002), pp. 2166–2175. DOI: 10.1109/TMTT.2002.802331.

[28] D. Schurig, J. J. Mock, B. J. Justice, S. A. Cummer, J. B. Pendry, A. F. Starr, and D. R. Smith. "Metamaterial Electromagnetic Cloak at Microwave Frequencies." In: *Science* 314.5801 (2006), pp. 977–980. ISSN: 0036-8075. DOI: 10.1126/science.1133628. eprint: https://science.sciencemag.org/content/314/5801/977.full.pdf. URL: https://science.sciencemag.org/content/314/5801/977.

[29] D. Sievenpiper, Lijun Zhang, R. F. J. Broas, N. G. Alexopolous, and E. Yablonovitch. "High-impedance electromagnetic surfaces with a forbidden frequency band." In: *IEEE Transactions on Microwave Theory and Techniques* 47.11 (1999), pp. 2059–2074. DOI: 10.1109/22.798001.

[30] John Thornton and Kao-Cheng Huang. *Modern lens antennas for communications engineering*. Wiley, 2013.

[31] Xingcun Colin Tong. "Concepts From Metamaterials to Functional Metadevices." In: *Functional Metamaterials and Metadevices*. Cham: Springer International Publishing, 2018, pp. 1–21. ISBN: 978-3-319-66044-8. DOI: 10.1007/978-3-319-66044-8_1. URL: https://doi.org/10.1007/978-3-319-66044-8_1.

[32] Fan Yang and Yahya Rahmat-Samii. *Electromagnetic Band Gap Structures in Antenna Engineering*. eng. The Cambridge RF and microwave engineering series. Cambridge: Cambridge University Press, 2008. ISBN: 052188991X.

[33] Ang Yu, Fan Yang, Atef Z. Elsherbeni, John Huang, and Yahya Rahmat-Samii. "Aperture efficiency analysis of reflectarray antennas." In: *Microwave and Optical Technology Letters* 52.2 (2010), pp. 364–372. DOI: https://doi.org/10.1002/mop.24949. eprint: https://onlinelibrary.wiley.com/doi/pdf/10.1002/mop.24949. URL: https://onlinelibrary.wiley.com/doi/abs/10.1002/mop.24949.